Available online at www.sciencedirect.com

SCIENCE DIRECT®

Remote Sensing of Environment 94 (2005) 384–404

Remote Sensing of Environment

www.elsevier.com/locate/rse

Seasat—A 25-year legacy of success

Diane L. Evans[a,*], Werner Alpers[b], Anny Cazenave[c], Charles Elachi[a], Tom Farr[a], David Glackin[d], Benjamin Holt[a], Linwood Jones[e], W. Timothy Liu[a], Walt McCandless[f], Yves Menard[g], Richard Moore[h], Eni Njoku[a]

[a]*Jet Propulsion Laboratory, California Institute of Technology, Pasadena, CA 91109, United States*
[b]*Universitaet Hamburg, Institut fuer Meereskunde, D-22529 Hamburg, Germany*
[c]*Laboratoire d'Etudes en Geophysique et Oceanographie Spatiales, Centre National d'Etudes Spatiales, Toulouse 31401, France*
[d]*The Aerospace Corporation, Los Angeles, CA 90009, United States*
[e]*Central Florida Remote Sensing Laboratory, University of Central Florida, Orlando, FL 32816, United States*
[f]*User Systems Enterprises, Denver, CO 80220, United States*
[g]*Centre National d'Etudes Spatiales, Toulouse 31401, France*
[h]*The University of Kansas, Lawrence, KS 66047-1840, United States*

Received 10 June 2004; received in revised form 13 September 2004; accepted 16 September 2004

Abstract

Thousands of scientific publications and dozens of textbooks include data from instruments derived from NASA's Seasat. The Seasat mission was launched on June 26, 1978, on an Atlas-Agena rocket from Vandenberg Air Force Base. It was the first Earth-orbiting satellite to carry four complementary microwave experiments—the Radar Altimeter (ALT) to measure ocean surface topography by measuring spacecraft altitude above the ocean surface; the Seasat-A Satellite Scatterometer (SASS), to measure wind speed and direction over the ocean; the Scanning Multichannel Microwave Radiometer (SMMR) to measure surface wind speed, ocean surface temperature, atmospheric water vapor content, rain rate, and ice coverage; and the Synthetic Aperture Radar (SAR), to image the ocean surface, polar ice caps, and coastal regions. While originally designed for remote sensing of the Earth's oceans, the legacy of Seasat has had a profound impact in many other areas including solid earth science, hydrology, ecology and planetary science.

Keywords: Seasat; Scanning Multichannel Microwave Radiometer; Synthetic Aperture Radar

1. Introduction

The Seasat mission was designed to demonstrate the feasibility of global satellite monitoring of oceanographic phenomena and to help determine the requirements for an operational ocean remote sensing satellite system. Specific objectives were to collect data on sea-surface winds, sea-surface temperatures, wave heights, ocean topography, internal waves, atmospheric water, and sea ice properties.

Requirements for Seasat were generated by a User Working Group (UWG), which included the Office of the Oceanographer of the U.S. Navy, Fleet Numerical Weather Center in Monterey, CA, Navy Surface Weapons Center in Dahlgren, VA, Naval Research Laboratory, the Johns Hopkins University Applied Physics Laboratory (APL), the Office of Naval Research, and the Navy/NOAA Joint Ice Center. NOAA was represented on the UWG by the many NOAA laboratories around the nation, including the NOAA Atlantic Oceanic Marine Laboratory (AOML) in Miami, FL, the NOAA weather center in Suitland, MD, the NOAA Pacific Marine Environmental Laboratory in Seattle, WA,

* Corresponding author. Tel.: +1 818 354 2418; fax: +1 818 393 3379.
E-mail addresses: diane.evans@jpl.nasa.gov (D.L. Evans), alpers@ifm.uni-hamburg.de (W. Alpers), anny.casenave@cnes.fr (A. Cazenave), charles.elachi@jpl.nasa.gov (C. Elachi), tom.farr@jpl.nasa.gov (T. Farr), David.L.Glackin@aero.org (D. Glackin), ben@pacific.jpl.nasa.gov (B. Holt), ljones@pegasus.cc.ucf.edu (L. Jones), liu@pacific.jpl.nasa.gov (W.T. Liu), waltmc@usersystems.com (W. McCandless), yves.menard@cnes.fr (Y. Menard), rmoore@sunflower.com (R. Moore), eni.njoku@jpl.nasa.gov (E. Njoku).

doi:10.1016/j.rse.2004.09.011

and NOAA's Marine Fisheries office in Bay St Louis, MS. The Defense Mapping Agency, United States Geological Survey (USGS), the U.S. Coast Guard, and the Department of the Interior were also represented on the UWG. As the applications planning program matured, a wide range of commercial users, including ship routing services, offshore oil and gas industries, fisheries, mining and other participants joined the UWG to plan experiments for the Seasat Program.

Four complementary microwave experiments were onboard to return the maximum information from ocean surfaces. The Radar Altimeter (ALT) measured ocean topography and wave heights by measuring spacecraft altitude above the ocean surface. The experiment operated at Ku-band (13.5 GHz) and had 10 cm vertical accuracy. The Seasat-A Satellite Scatterometer (SASS) was used to measure wind speed and direction over the ocean. SASS operated at Ku-band (14.6 GHz) and provided accuracies of better than ± 2 m/s (speed) and 20° (direction). The Scanning Multichannel Microwave Radiometer (SMMR) was used to measure surface wind speed (± 2 m/s), ocean surface temperature (± 2 °C), atmospheric water vapor content, rain rate, and ice coverage. The instrument was passive, and operated at 6.6, 10.7, 18, 21, and 37 GHz with a 600-km swath width. The Synthetic Aperture Radar (SAR) was designed to image the ocean surface (wave patterns), polar ice, coastal regions, and land areas. The SAR operated at L-band (1.275 GHz), at a single polarization of horizontal transmit-horizontal receive (HH), and a fixed 100 km swath with incidence angles of 20–26° and resolution of 25 m. The National Oceanic and Atmospheric Administration (NOAA) provided a fifth instrument to the Seasat Mission, a visible and infrared radiometer (VIRR) from their weather satellite program to provide surface mapping that could be compared to the data from the other sensors.

Seasat was launched on June 26, 1978, on an Atlas-Agena rocket from Vandenberg Air Force Base and was injected into a near-circular polar orbit (108° inclination) with an apogee of 798 km and a perigee of 775 km. The mission ended suddenly on October 10, 1978 due to a failure of the satellite's electric power system. The instantaneous data rate of 120 Mbps of the SAR data exceeded the capabilities of the available onboard tape recorders of that era and could only be collected when the satellite was in view of the specially equipped ground stations. NASA supplied stations near Fairbanks, AK, Cape Canaveral, FL and Goldstone, CA. The Canadian Centre for Remote Sensing (CCRS) provided a station in St. Johns, Newfoundland and the European Space Agency (ESA) provided a station near London in the United Kingdom. Although limited Seasat data were acquired, the mission not only demonstrated the feasibility of using microwave sensors to monitor ocean and land conditions, but also laid the groundwork for many future missions. This paper presents an overview of the still-highly innovative Seasat mission and its compelling legacy.

2. Radar altimeter (ALT)

2.1. Instrument characteristics, heritage, and legacy instruments

Prior to Seasat, proof-of-concept missions were flown during the 1970s, beginning with an altimeter that operated on Skylab for over 5 months in 1973 and 1974, and the GEOS-3 altimeter that operated with intermittent temporal and geographical coverage from 1975 to 1978 (Table 1). This proof-of-concept phase culminated with the Seasat Radar Altimeter (ALT), which was derived from the GEOS-3 altimeter but had improved accuracy. The Seasat ALT was provided by NASA's Wallops Flight Center and the Johns Hopkins University Applied Physics Laboratory. The instrument characteristics are shown in Table 2.

After Seasat, the U.S. Navy launched the Geosat altimeter in March 1985, based largely on the Seasat altimeter design for the primary purpose of high-resolution

Table 1
Altimeter summary (Glackin, 2004; Glackin & Peltzer, 1999; Kramer, 2001)

Platform	Instrument	Country or agency	Frequencies (GHz)	1HZ sea-level measurement accuracy (cm)	Pulse limited footprint (km)	Orbit alt (km)	Launch date
Skylab	S-193	USA	13.9	90	8	435	May 1973
GEOS-3	ALT	USA	13.9	20/50	3.5	838	April 1975
Seasat	ALT	USA	13.5	10	1.7	799	June 1978
Geosat	Radar Alt	USA	13.5	5	1.7	800	March 1985
ERS-1	RA-1	ESA	13.8	5 to 7	1.7	784	July 1991
TOPEX/Poseidon	ALT, SSALT	USA/France	5.3/13.6	4.2	2.2	1336	August 1992
ERS-2	RA-1	ESA	13.8	5 to 7	1.7	784	April 1995
Mir-Priroda	Greben	Russia	13.8	10	2.3	400	April 1996
Geosat follow-On	RA	USA	13.5	3.5	2	800	February 1998
Jason-1	Poseidon-2	France/USA	5.3/13.6	3.3	2.2	1336	December 2001
ENVISAT	RA-2	ESA	3.2/13.6	4.5	1.7	800	March 2002
CryoSat	SIRAL	ESA	5.3/13.6	5 to 7	1.6	720	2005[a]
Jason-2/OSTM		France/USA	5.3/13.6	3.3	2.2	1336	2008[a]

[a] Estimated.

Table 2
Seasat ALT summary (Townsend, 1980)

Satellite altitude	800 km
Frequency	13.5 GHz
Range resolution	10 cm
Beam-limited footprint	22.2 km
Pulse-limited footprint	1.7 km
Antenna type	1 m diameter parabola, nadir-pointed
Antenna gain	41 dB
RF bandwidth	320 MHz chirp pulse bandwidth
Transmit pulse length	3.2 μs
Pulse repetition freq	1020 pps
TWTA power	2 kW
Transmitted power	6.5 W

mapping of the global marine geoid for military applications. Upon completion of the geoid-mapping objective, Geosat was maneuvered into the Seasat orbit in September 1986 and continued to operate until October 1989. The European Space Agency has subsequently operated single-frequency altimeters since July 1991 onboard the Earth Remote Sensing satellites ERS-1 and ERS-2, and ENVISAT.

TOPEX/Poseidon (T/P), launched in August 1992 by the U.S. National Aeronautics and Space Administration (NASA) and the French space agency Centre National d'Etudes Spatiales (CNES), is the first dedicated satellite altimeter mission optimally designed for scientific study of the ocean. Compared with its predecessors, the instrumental measurement accuracy of the dual-frequency altimeter onboard T/P improved by more than a factor of two and the orbit accuracy improved by more than an order of magnitude, resulting in an overall measurement accuracy of about 4 cm rms for a single ground trace (Chelton, 2001). Such a performance makes it possible to detect 1 cm change in sea level at a regional scale and to monitor changes in global mean sea level to about 2 mm/year.

On December 7, 2001, the NASA/CNES Jason-1 mission was launched as a follow-on to TOPEX/Poseidon (Fig. 1). Since July 2002, Jason and TOPEX/Poseidon have flown in tandem offering a much-improved sampling capability for the study of ocean circulation and tides (Fig. 2). Further improvements in spatial resolution may be expected by combining the ENVISAT and Geosat Follow-on (GFO) data sets (Fu et al., 2003).

2.2. Altimeter geophysical measurements

Seasat and its legacy of altimeter missions have clearly demonstrated the wide range of potential oceanographic and geophysical applications of altimetric measurements of ocean topography (Fu & Cazenave, 2001).

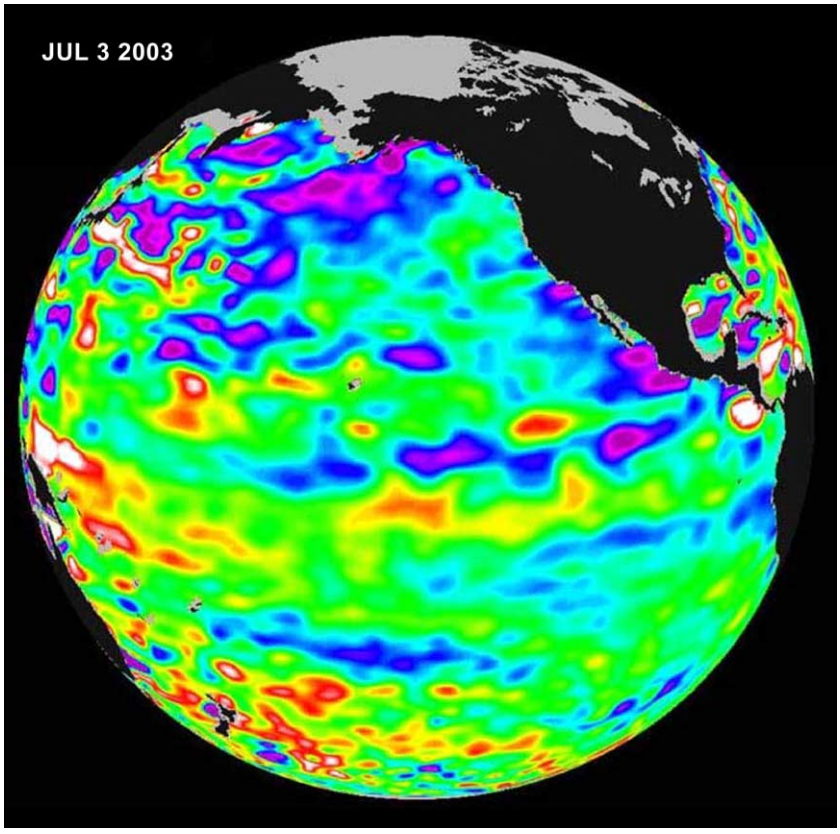

Fig. 1. Jason data taken during a 10-day collection cycle ending July 3, 2003. Red areas are about 10 cm above normal, white areas show the sea-surface height is between 14 and 32 cm above normal. The blue areas are between 5 and 13 cm below normal, and the purple areas range from 14 to 18 cm below normal. Data such as these are now used routinely for predictions of such phenomena as El Niño and Pacific Decadal Oscillation.

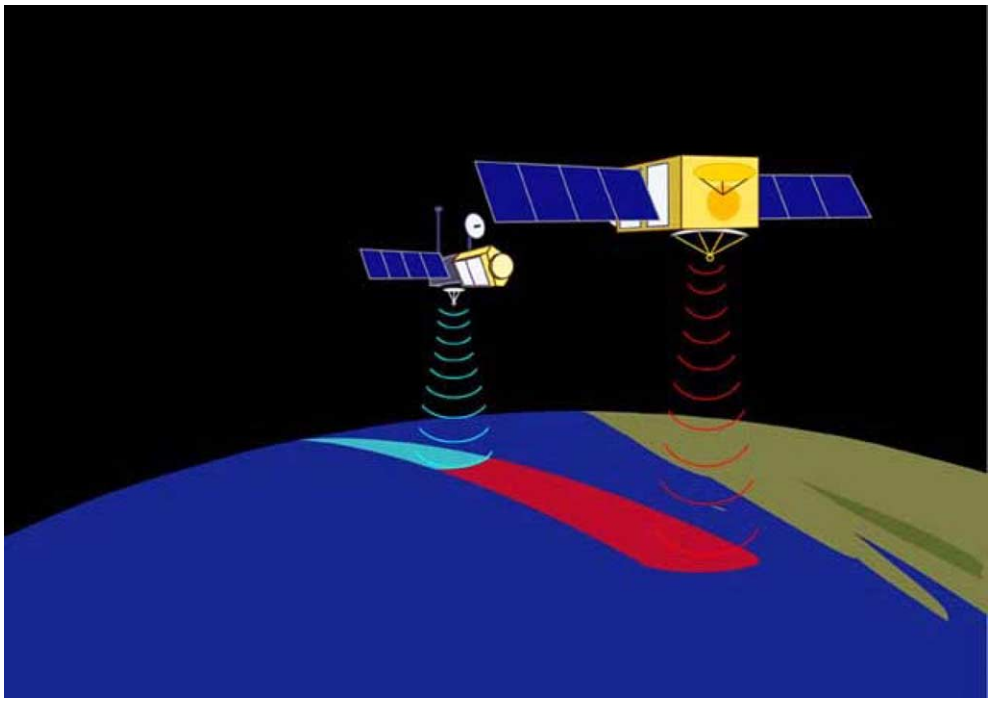

Fig. 2. Artist's concept of Jason and TOPEX/Poseidon working in tandem.

Seasat altimeter, thanks to the unprecedented performance of measuring sea level to an accuracy of few centimeters, was the first altimeter that provided a synoptic view of the ocean surface with details, which were never seen before (Fig. 3). This instrument has to be considered as a pioneer in many fields, but in particular it produced a clear demonstration of the unique contribution of altimetry for measuring and monitoring of ocean dynamics. For the first time, in just a few weeks of observation, not only was complete ocean meso-scale variability observed in the highly turbulent western boundary current regions (Cheney & Marsh, 1981; Menard, 1983), but also globally (Cheney et al., 1983; Fu, 1983; Fig. 3). Because of the limited sampling of the conventional in situ observations, the importance of the short-term, short-scale variability in the ocean was not known. The Seasat altimeter highlighted the essential role of the fast-moving eddy field in the ocean energy transport and the heat exchange with the atmosphere.

The Geosat, ERS1-2, TOPEX/Poseidon, GFO, and Jason-1 missions have continued to revolutionize our view of the oceans. Each of these altimeter missions was a direct outgrowth of the Seasat altimeter. After about 10 years of intense research, many scientists around the world developed dedicated processing techniques and made essential discoveries in oceanography using the short 3-month long time series of Seasat altimetric data. In addition to meso-scale variability, Seasat altimetry was the initiator of major progress in a description of the mean ocean circulation (Wunsch & Gaposchkin, 1980), in tide modeling (Mazzega, 1985), in significant wave height and wind speed monitoring (Chelton et al., 1981), in swell propagation (Mognard et al., 1983), and in many other areas (see, for instance, the Journal of Geophysical Research special issue, February 1983). The powerfulness of dynamic sea-surface topography as measured by radar altimetry was also demonstrated through the first assimilation experiments in 3D ocean models (De Mey & Menard, 1989). Indeed, because it is representative of changes in dynamics from the surface to the deeper layers, sea-surface topography has had an essential impact on improved models and forecast.

Since Seasat, altimetry has become indispensable for looking at the different space–time scales of the ocean variability, from a few days to a few years, from a few tens to thousands of kilometers. It is considered a key component of the operational ocean analysis and forecast centers. These centers provide valuable products for offshore industry, ship routing, ocean pollution monitoring, ecosystem surveys, marine meteorology and climate forecasting. However, these centers depend upon continued altimetric data flow to carry on their missions. The Jason-2/Ocean Surface Topography Mission (OSTM) satellite should provide a follow-on for the Jason-1 mission in 2008, but high-resolution sampling is required in future missions to go further. Altimeter data continuity is essential to maintain the progress that began over 25 years ago with Seasat.

Maps of sea level made by Seasat revolutionized knowledge of the marine geoid, allowing detailed studies of the processes influencing the geoid at all wavelengths. The Seasat maps reduced the errors in the geoid from 3 to 10 m or larger in even the best mapped regions, to less than 1 m. More importantly, the maps have a much-improved resolution of tens of centimeters in the vertical and 18–100 km horizontally, showing the fine structure of the geoid in

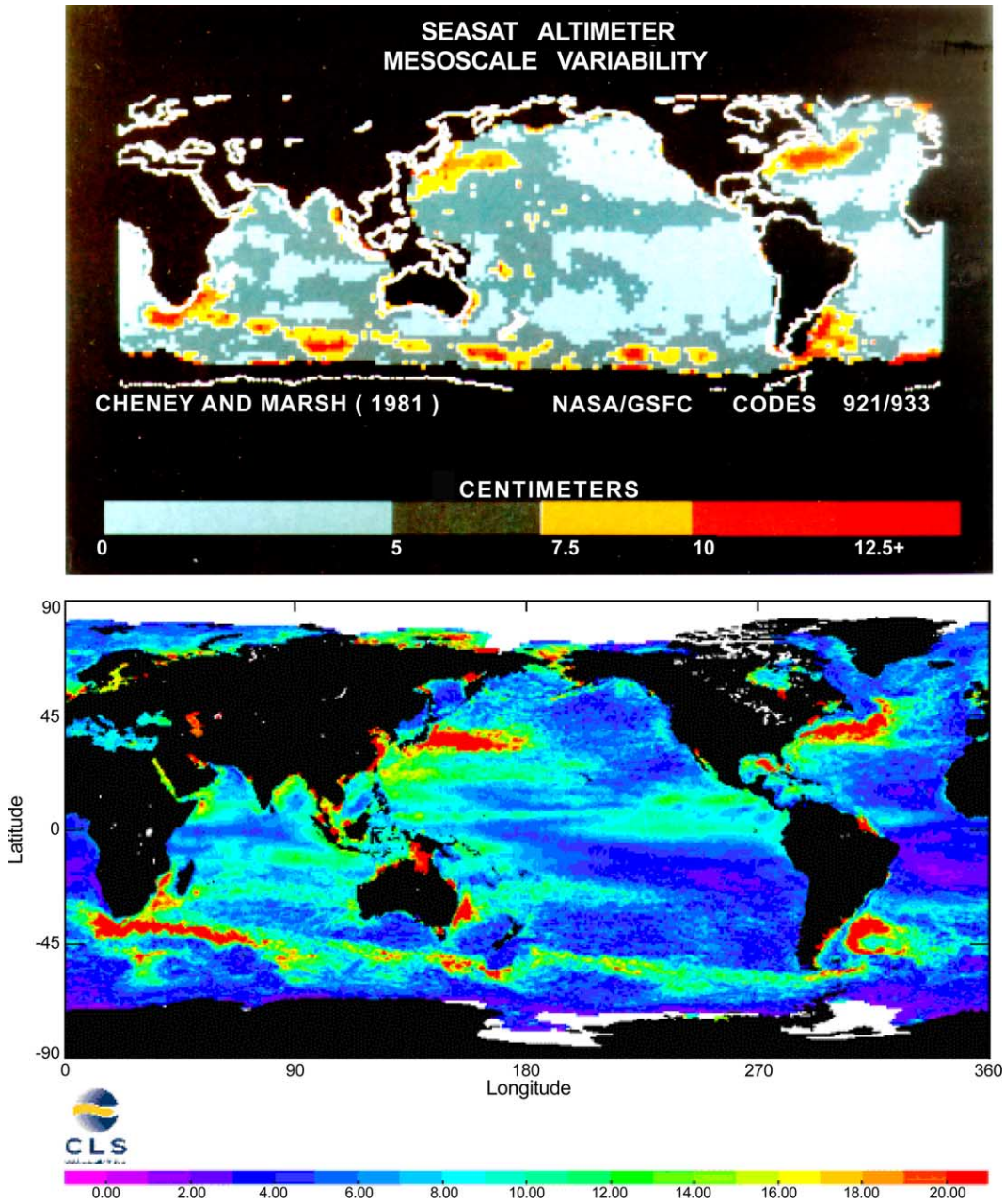

Fig. 3. Seasat (top) provided the first global view of the ocean dynamics. TOPEX/Poseidon sea-surface topography is shown in the bottom panel.

unprecedented detail, especially in areas of the Southern Hemisphere that had been poorly surveyed by ships (Stewart, 1988). Although altimeter data still dominates the shortest wavelength (tens of kilometers) gravity knowledge, the long and medium wavelength information has been revolutionized by the launch of the joint NASA–German Aerospace Center Gravity Recovery and Climate Experiment (GRACE) mission in March 2002. Using just a few months of globally uniform quality GRACE data, it has been possible to improve the accuracy of Earth's gravity model by a factor of between 10 and nearly 100, depending on the size of the gravity feature. In some locations, errors in geoid height based upon previous data of as much as 1 m have been reduced to the centimeter level.

In the polar regions, the elevation-measuring capabilities of the Seasat altimeter were also applied to the polar ice sheets of Greenland and Antarctica, to estimate mass balance and slope changes in ice shelves (Zwally & Brenner, 2001). Improvements in the waveform tracking over land were made on the ERS-1/2 altimeters, leading to time series studies of elevation change (Wingham et al., 1998; Zwally et al., 2002a). Such studies are expected to continue with NASA's laser altimeter on the Icesat mission launched in early 2003, the ENVISAT altimeter, and ESA's upcoming CryoSat radar altimeter mission to be launched in 2005 (Wingham, 1999). Mass balance studies have been combined with gravity measurements (such as GRACE) to provide insight on past impacts of glacial periods (Wu et al.,

2002). Using the same instruments, the measurement of sea ice freeboard (the portion of sea ice that extends above sea level) has also been examined with radar altimeters (e.g., Laxon et al., 2003) and, along with ice sheets, is a primary objective of the CryoSat mission.

3. Seasat-A Satellite Scatterometer (SASS)

3.1. Instrument characteristics, heritage, and legacy instruments

The first spaceborne instrument useful for demonstrating scatterometry was flown on the NASA Skylab missions in 1973 to 1974 (Moore et al., 1974; Table 3), but it was not until the NASA Seasat mission in 1978 that a microwave scatterometer instrument was designed specifically for wind observations. SASS demonstrated that accurate measurements of wind velocity could be obtained from spaceborne scatterometers and allowed construction of the first accurate, basin-scale, 100-km-resolution maps of synoptic surface winds over the ocean.

SASS consisted of four fan-beam, dual-polarized antennas, oriented at 45° and 135° to the spacecraft subtrack, illuminated two 500-km swaths, one on each side of the spacecraft, that provided wind vectors at 50-km resolution (Table 4). However, only one side was in operation most of the time, covering less than 40% of the global ocean daily. The incidence angle varied from 25° to 55°. The precision of the backscatter returns was about 0.7 db. The two orthogonal azimuth angles were not able to unambiguously resolve the wind direction in all conditions (Liu, 2002).

Scatterometers have flown on NASA and ESA research missions continuously since 1991. These missions have provided near-real-time data that have been used in operational numerical weather prediction and marine forecasting. The ERS-1 mission was launched on July 17, 1991, with the scatterometer turned off in June of 1996. The essentially identical follow-on ERS-2 mission was launched April 21, 1995 and is still operating nominally except that scatterometer wind production was suspended due to failure on the gyroscope and onboard tape recorder. Although initially, the ERS-1 wind products did not meet the prelaunch specifications (Stoffelen & Anderson, 1997), algorithm and processing refinements led by investigators at ECMWF yielded accurate vector wind products within about 18 months after launch. ECMWF began routine assimilation of ERS wind products in May 1996.

Table 4
Seasat SASS summary (Johnson et al., 1980)

Satellite altitude	800 km
Frequency	14.6 GHz (Ku band)
Polarization	VV, HH
Spatial resolution	50 km
Swath width	2×500 km (one swath on each side of S/C subtrack)
Antenna type	Four fan-beam stick antennas
Transmit pulse length	4.8 μs
Transmitter duty factor	17%
Transmitter peak power	100 W

On the basis of the SASS results, NASA initiated the NASA Scatterometer (NSCAT) project for designing and building a dual-swath, Ku-band scatterometer instrument and an associated NASA ground data processing and distribution system to service the research community. After many delays, an international collaboration was arranged to fly NSCAT as a U.S. contribution to the Japanese National Space Development Agency's (NASDA's) Advanced Earth Observation Satellite (ADEOS-I) research mission.

ADEOS-I was launched on August 17, 1996, and NSCAT measurements were available nearly continuously from mid-September 1996 until the abrupt failure of the spacecraft's solar panel on June 30, 1997. Validated near-real-time data were made available by NOAA/NESDIS starting in February 1997. Assimilation of NSCAT vector wind data into the Goddard Earth Observing System (GEOS-2) resulted in a 24-h extension of useful forecast skill in the Southern Hemisphere extratropics, with more modest impacts in the Northern Hemisphere extratropics (Atlas et al., 2001).

Following the premature failure of ADEOS-I and the loss of NSCAT data, NASA initiated the rapid-development QuikSCAT mission to minimize the gap in broadswath scatterometer data between NSCAT and SeaWinds/ADEOS-II. QuikSCAT utilized an off-the-shelf satellite bus and existing SeaWinds flight hardware and spares prepared for ADEOS-II; the mission was ready to launch approximately

Table 3
Wind scatterometer summary (Glackin, 2004; Glackin & Peltzer, 1999; Kramer, 2001)

Platform	Instrument	Country or agency	Band	Frequency (GHz)	Polarization	Spatial res (km)	Swath width (km)	Orbit (km)	Alt launch date
Skylab	S-193	USA	Ku	13.9	VV, HH	16	180	435	May 1973
Seasat	SASS	USA	Ku	14.6	VV, HH	50	2×500	799	June 1978
ERS-1	AMI (Wind)	ESA	C	5.3	VV	50	500	784	July 1991
ERS-2	AMI (Wind)	ESA	C	5.3	VV	50	500	784	April 1995
ADEOS	NSCAT	USA	Ku	14.0	VV, HH	25/50	2×600	798	April 1996
QuikSCAT	SeaWinds	USA	Ku	13.4	VV, HH	50	1800	800	June 1999
ADEOS-2	SeaWinds	USA	Ku	13.4	VV, HH	50	1800	806	December 2002
MetOp-1	ASCAT	ESA/EUMETSAT	C	5.2	VV	50	2×550	720	2005[a]

[a] Estimated.

18 months after the demise of ADEOS-I, although the actual launch was delayed, owing to launch vehicle problems, until June 1999. Scatterometer data were obtained starting in July 1999, and validated near-real-time data were produced routinely by European Centre for Medium-Range Weather Forecasts and NOAA/NESDIS (using NASA-provided software) starting in early 2000. As with NSCAT, these data are provided to marine forecast offices in graphical form and to major national and international forecast centers for assimilation into numerical weather prediction systems.

The second SeaWinds scatterometer instrument was launched from Japan's Tanegashima Space Center on December 13, 2002 on the ADEOS-II (renamed MIDORI-2 at launch) spacecraft and flew in tandem with QuikSCAT until October 24, 2003, when the spacecraft irrecoverably lost power. The tandem mission provided over 60% global coverage in 6 h and 90% in 12 h (Liu, 2003). Global ocean-surface vector winds information at this frequency is essential for resolving diurnal and locally varying winds that drive ocean mixing and transport processes. Tandem operations also increase detection of tropical storms (e.g., Fig. 4).

3.2. Scatterometer geophysical measurements

The SASS was a proof-of-concept experiment for measuring ocean surface wind vectors under day/night near-all-weather conditions. The physical basis for this remote sensing technique is the generation of capillary waves on the ocean surface by the friction velocity of the wind. The amplitude of these centimeter-wavelength ocean waves is in equilibrium with the local wind, and the two-dimensional wave spectrum is highly anisotropic with the wind direction. The ocean radar backscatter results from Bragg scattering from these capillary waves, and the normalized radar cross section (sigma-0) grows approximately as a power series of wind speed (Moore & Fung, 1979).

The SASS made backscatter measurements at two azimuth directions (separated by 90°) to determine both the magnitude of the wind speed and its direction. The wind vector retrieval algorithm (Jones et al., 1978; Wentz, 1991) used an empirically derived statistical relationship known as the scatterometer geophysical model function (GMF; Schroeder et al., 1982; Wentz et al., 1984), to relate the ocean sigma-0 to the frictional wind speed. Because the GMF was largely the second harmonic of the relative wind direction, the wind retrieval inferred multiple possible wind vectors. Since SASS was a proof-of-concept mission, the closest wind direction to "surface truth" was chosen for evaluation. Geophysical validation of SASS measurements used ocean buoys, research ships, and meteorological analysis wind fields (Jones et al., 1982). Results demonstrated that the SASS successfully met its goal of measuring wind speed better than ±2 m/s and ±20° rms direction. Follow-on scatterometers, European Remote Sensing Satellite Active Microwave Instrument (Attema, 1991) and NASA Scatterometer (Naderi et al., 1991), and SeaWinds were modified to provide three azimuth looks (four for SeaWinds), which enabled the correct wind direction to be selected with high accuracy using instrument skill (Naderi et al., 1991).

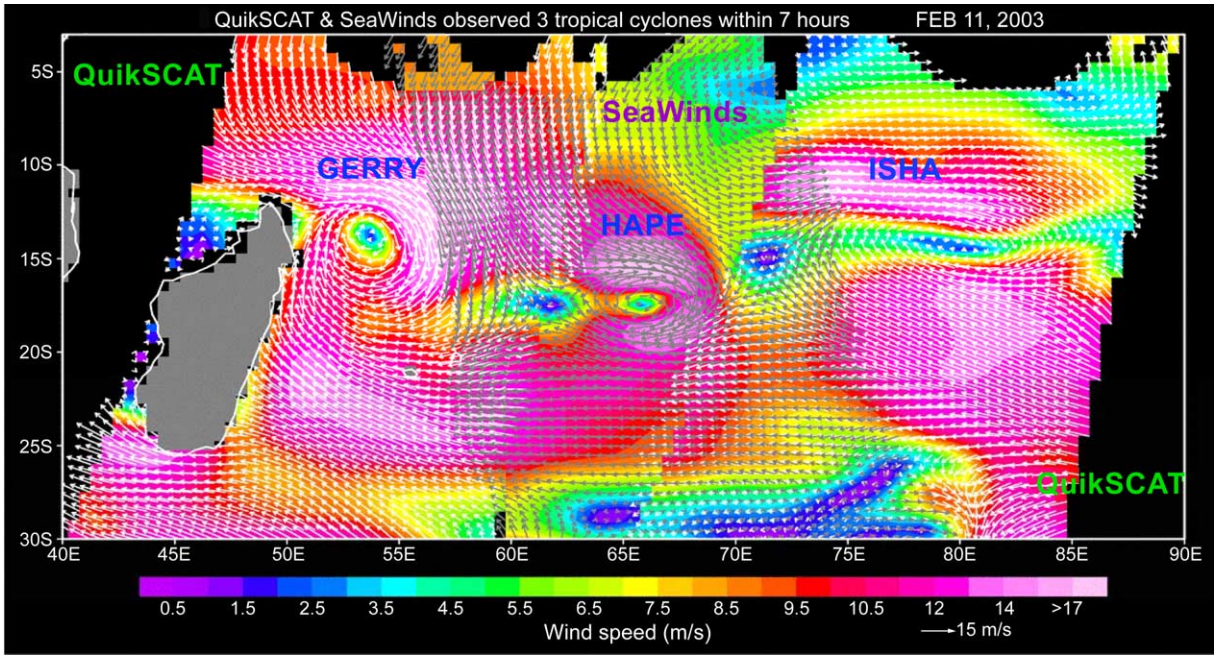

Fig. 4. QuikSCAT and SeaWinds Tandem data collected on January 28 and 29, 2003. Continents are shown in green, polar glacial ice-covered regions in blue-red and sea ice in gray. Color and intensity changes over ice and land are related to ice melting, variations in land surface roughness and vegetation cover. Ocean surface wind speeds, measured during a 12-h period on January 28, are shown by colors. Blues correspond to low wind speeds and reds to wind speeds up to 15 m per second. Black arrows denote wind direction. White gaps over the oceans represent unmeasured areas between SeaWinds swaths (the instrument measures winds over about 90% of the oceans each day).

In the years following the demise of Seasat, SASS wind vector measurements were evaluated by scientists for use in ocean circulation models, air–sea flux studies, numerical weather forecasting, and many varied applications (Liu, 2002). While SASS data were never used for operational numerical weather prediction or marine forecasting, since near-real-time telemetry was not available, and geophysical processing algorithms were not in place at launch, investigations into the operational utility of future scatterometer data were initiated as soon as SASS wind velocity data became available.

Scatterometer data are being used in an increasing number of land applications. These applications include monitoring of changes in soil moisture (Magagi & Kerr, 2001; Macelloni et al., 2003); monitoring of vegetation (Long & Hardin, 1994; Long et al., 2001; Hardin & Jackson, 2003); and detection of regional flooding (Brakenridge et al., 2002; Nghiem et al., 2003). In the polar regions, scatterometer backscatter maps have been shown to be of considerable value. SASS measurements were found to be sensitive to the seasonal melt cycle in the polar regions, including sea ice (Carsey, 1985), ice sheets and snow on land, with the timing and duration of melt cycles likely being responsive to climatic temperature variations. Making use of this sensitivity, scatterometer time series studies have identified the extent of seasonal snowmelt zones over Antarctica (Bingham & Drinkwater, 2000) and Greenland (Wismann, 2000a), including estimates of snow accumulation (Drinkwater et al., 2001). Snowmelt studies have been extended to freeze–thaw cycles in the boreal forests (Kimball et al., 2001) and over land (Wismann, 2000b), which when combined with the longer passive microwave record, are indicating the date of thaw onset to be earlier and earlier in time. The freeze–thaw cycle in the boreal forests is a primary science driver in the combined active–passive Hydrosphere State Mission (HYDROS) mission (Entekhabi et al., 2003). Key sea ice applications include routine generation of sea ice motion maps (Zhao et al., 2002), of value for determining the heat flux between the ocean and atmosphere, and the assessment of changes in the extent of the perennial and seasonal ice packs in the Arctic (Kwok et al., 1999). Both measurements provide a means for assessing polar climate change, particularly related to the large-scale transport of ice in response to shifting atmospheric oscillations and subsequent impacts on ice thickness. (e.g., Abdel-Messeh & Quegan, 2000; Kennett & Li, 1989; Wagner et al., 2003; Woodhouse & Hoekman, 2000).

4. Scanning multichannel microwave radiometer (SMMR)

4.1. Instrument characteristics, heritage, and legacy instruments

The Scanning Multichannel Microwave Radiometer (SMMR) was flown on both the Seasat and Nimbus-7 missions (Table 5). Nimbus-7 was launched on October 24,

Table 5
Microwave conically scanning surface imager sensor heritage[a] (Glackin, 2004; Glackin & Peltzer, 1999; Kramer, 2001)

Instrument	Frequencies (GHz)	Antenna diameter (m)	Incidence angle (°)	Orbit altitude (km)	Swath width (km)	Launch date
SMMR (Seasat)	6.6, 10.7, 18, 21, 37	0.8	48.8	794	600	June 1978
SMMR (Nimbus-7)	6.6, 10.7, 18, 21, 37	0.8	50.3	955	780	October 1978
SSM/I (DMSP 5D-2 series)	19.3, 22.2, 37, 85.5	0.6	53.1	830	1400	July 1987
IKAR-P (Mir-Priroda)	13.0, 22.3, 36.5	0.7	~43.1	~400	680	April 1996
TMI (TRMM)	10.65, 19.3, 21.3, 37.0, 85	0.6	53.1	350	780	November 1997
MSMR (IRS-P4)	6.6, 10.7, 18, 21	0.8	49.7	720	1360	May 1999
SeaWinds[b] (QuikSCAT)	13.4	1.0	54	803	1800	June 1999
Delta-2D (Okean-O)	6.9, 13.0, 22.3, 37.5	0.7	~45.0	~635	1130	July 1999
AMSR-E (Aqua)	6.9, 10.7, 18.7, 23.8, 36.5, 89	1.6	55	705	1445	May 2002
SeaWinds[b] (ADEOS-II)	13.4	1.0	54	803	1800	December 2002
AMSR (ADEOS-II)	6.9, 10.7, 18.7, 23.8, 36.5, 50.3, 52.8, 89	2.0	55	803	1600	December 2002
SSMIS (DMSP_5D-3 series)	24 channels from 19 to 183	0.6	53.1	833	1700	October 2003
WindSat (Coriolis)	6.8, 10.7, 18.7, 23.8, 37	1.8	55	830	1025	January 2003
MIMR (FY-3 series)	10.65, 18.7, 23.8, 36.5, 89, 150		53	836	1400	2005[c]
MSMR/improved (IRS-P7)	Characteristics undefined at present					2006[c]
MADRAS (Megha-Tropiques)	18.7, 23.8, 36.5, 89, 157		53	867	1700	2006[c]
GPM-Core	10.65, 18.70, 23.8, 36.5, 89.0	TBD	TBD	400	TBD	2010[c]
CMIS (NPOESS)	6 to 190 (77 channels)	2.2	53	833	1700	2009[c]
HYDROS[d]	1.26, 1.41	6.0	40	670	1000	2010[c]

[a] Passive sensors (radiometers) except as indicated. (Note that the Aquarius and SMOS missions are not listed, because they do not employ conically scanning instruments. See Section 4.1 for more details.)
[b] Radar.
[c] Estimated.
[d] Radar-radiometer.

1978, and acquired imaging data for over 8 years until the scan mechanism was shut down in August 1987. The instrument was conceived and managed by the Goddard Space Flight Center, and built by the Jet Propulsion Laboratory. It was designed to measure parameters of the ocean, atmosphere, and cryosphere using five frequency bands centered at 6.6, 10.7, 18, 21, and 37 GHz. The instrument capabilities were a significant advancement over those of earlier spaceborne radiometers, in terms of spatial resolution, accuracy, number of measurement channels, and diversity of parameters measured (Gloersen & Barath, 1977; Njoku et al., 1980). Over the ocean, the SMMR measured surface temperature, surface wind speed, precipitable water, integrated cloud liquid water, and rain rate. Cryospheric parameters measured were sea ice extent and concentration, and snow cover extent. Over land, the SMMR provided information on precipitation, soil moisture, and vegetation cover. The data and validation results from the two SMMR instruments provided a wealth of engineering and scientific discovery, far exceeding the original expectations.

In addition to its provision of key ocean and atmospheric measurements, the SMMR was included in the Seasat complement of sensors to provide needed atmospheric path length corrections for the altimeter instrument, and atmospheric attenuation corrections for the Scatterometer instrument. In this sense, the Seasat mission broke new ground in the use of synergistic microwave measurements. The Seasat mission was the first to operate a multifrequency microwave imaging radiometer simultaneously with radar sensors on the same platform for remote sensing purposes, although the single-frequency scanning radiometer on Skylab (S-193) had flown along with the scatterometer and altimeter. This trend has continued with the water vapor and cloud liquid water radiometers flown with the altimeters on the TOPEX/Poseidon and JASON satellites, the synergistic flight of the AMSR and SeaWinds instruments on the ADEOS-II satellite, and the integrated radar-radiometer designs of the HYDROS missions (see Table 5). Also part of the SMMR legacy are the US/Argentinean Aquarius mission, designed to measure ocean salinity with a 3-beam pushbroom radiometer, planned for launch in 2008, and the European Soil Moisture Ocean Salinity (SMOS) mission, planned for launch in 2007. SMOS will use a thinned array radiometer to perform 2-D aperture synthesis, and will be the first such instrument to fly in space. (Aquarius and SMOS are not conically scanning radiometers and thus do not appear in Table 5).

The SMMR instrument characteristics are summarized in Table 6. The SMMR continued the earlier series of spaceborne radiometers and significantly advanced the development of microwave radiometry from space (Njoku, 1982). The earlier radiometers included instruments on the Cosmos 283 and 384 satellites, the NEMS and SCAMS atmospheric sounding instruments on the Nimbus-5 and -6 satellites, the ESMR surface imaging instruments on Nimbus-5 and -6, and the S-193 and S-194 instruments flown on the Skylab missions. The S-193 radiometer was a nonscanning scatterometer–radiometer instrument.

Table 6
SMMR characteristics (Njoku et al., 1980)

Center frequencies (GHz)	6.63	10.69	18	21	37
Sampling period (ms)	128	64	64	64	32
Sensitivity, ΔT (K)	0.7	0.8	0.9	1.0	1.4
Beamwidth (°)	4.5	2.9	1.8	1.5	0.93
IFOV (km)	135×87	87×56	54×35	45×29	28×18
Antenna aperture diameter (m)			0.79		
Scan period (s)			4.096		
Antenna offset angle (°)			42		
Earth-incidence angle (°)			48.8		
Swath width (km)			600		

Two new features introduced by the SMMR instrument were: (1) the increased number of simultaneous measurement channels (10) in the 6.6 to 37 GHz range (five frequencies, each dual-polarized) for surface and tropospheric sensing—two of these frequencies, 6.6 and 10.7 GHz, had not been available on previous radiometers; and (2) the conical-scan configuration, that enabled the surface to be viewed at a constant incidence angle across a relatively wide swath. The multichannel capability allowed several surface and atmospheric parameters to be measured simultaneously. This had significant advantages for estimating surface fluxes over the oceans and for synoptic analyses of storms and atmospheric fronts. The conical scan and constant incidence angle provided the advantage of minimizing the variability of incidence angle and footprint size across the swath, as error sources in the geophysical retrievals. It also increased the feasibility of using change detection to monitor land surface variability since this approach benefits from a consistent viewing geometry in repeat passes over the same target.

Because of these advantages, the multichannel conical-scanning configuration pioneered by the SMMR was adopted for subsequent spaceborne imaging (and some sounding) radiometers. These include the series of SSM/I, SSMIS, TMI, MSMR, AMSR, WindSat, Conical-scanning Microwave Imager/Sounder (CMIS), and HYDROS radiometer designs that have followed and improved upon the SMMR conceptual design (Table 5). The conical-scan configuration was also adopted later for scatterometry and was implemented in the SeaWinds sensors on the QuikSCAT and ADEOS-II satellites. The radiometers that followed the SMMR incorporated a number of design improvements that were a direct result of the SMMR experience. Among these improvements (starting with the SSM/I), the conical-scan design was modified such that the antenna rotated in azimuth through the full 360° rather than

oscillating sinusoidally as with the SMMR. In addition, the calibration targets were designed to be external to the main feed horn rather than having a separate cold sky horn and an internal hot load as with the SMMR. These engineering improvements resulted in subsequent radiometers delivering calibrated brightness temperature data of much improved polarization purity and calibration stability.

The WindSat instrument, launched on the Coriolis mission in 2003, is intended to determine if a passive microwave radiometer can measure not only sea-surface wind speed, but also direction, as a potential alternative to an active scatterometer. WindSat is fully polarimetric, in that it measures the complete Stokes vector using channels of various polarizations (Cunningham et al., 2004). WindSat is a risk reduction mission for the Conical-scanning Microwave Imager/Sounder (CMIS), slated to fly on all National Polar-orbiting Operational Environmental Satellite System (NPOESS) satellites. The intent for CMIS is to employ polarimetric microwave radiometry to measure sea-surface wind velocity operationally.

4.2. Passive microwave radiometer geophysical measurements

The SMMR measurement frequencies were designed for optimum sensitivity to specific surface and atmospheric parameters (Wilheit et al., 1980). The geophysical retrieval algorithms used subsets of the 10-channel measurements to derive the geophysical parameters, based on these sensitivities. The SMMR was the first imaging radiometer to include channels in the C- and X-band frequency ranges (6.6 and 10.7 GHz). These channels enabled the first measurements to be made of global sea-surface temperature and sea-surface wind speed using microwave radiometry (Bernstein & Morris, 1983; Black et al., 1985; Hofer et al., 1981). With its extended range of frequency channels, the SMMR also provided the first opportunity to measure ocean surface parameters simultaneously with key atmospheric parameters: precipitable water, cloud liquid water, and rainfall (Alishouse, 1983; Njoku & Swanson, 1983). The simultaneity of measurement of these parameters, which are key to determining fluxes of energy, moisture, and momentum at the ocean surface, provided a greatly improved capability for studies of air–sea interactions and ocean circulation (Katsaros & Brown, 1991; Liu & Niiler, 1984; McMurdie & Katsaros, 1985).

The SMMR near-all-weather, day and night capability provided a new opportunity for routine sea–ice and snow cover observations in polar regions. The multichannel SMMR data permitted discrimination of ice type as well as concentration, and the multiyear data set, including both SMMRs (Seasat and Nimbus-7), enabled valuable studies to be made of trends in sea ice extent (Parkinson & Gloersen, 1993). These studies have continued with the follow-on SSM/I sensors, and when including ESMR, provide now a 30-year time series of the polar regions. Starting in the late 1980s and continuing through the 1990s, the maximum (Parkinson & Cavalieri, 2002) and minimum (Comiso, 2002) Arctic sea ice extent has shown a consistent decrease, with at least some of these changes related to the positive nature of the Arctic and North Atlantic Oscillations indices during that time period. In comparison, the Antarctic sea ice cover has shown a slight increase in extent (Zwally et al., 2002b). Synergistic sea ice studies using combined SMMR and SAR data sets from Seasat also provided new insights into sea ice characterization and variability (Carsey, 1985; Carsey & Pihos, 1989). The multichannel capability of the SMMR provided the first opportunity to study snow cover extent and snow depth from space. Although not a focus of the Seasat mission, these measurements were an important legacy of the SMMR instrument (Foster & Chang, 1993). A serendipitous outcome of the SMMR, also not specifically related to the objectives of the Seasat mission, was the initiation of passive microwave monitoring of land surface vegetation and soil moisture from space (Choudhury et al., 1990; Kerr & Njoku, 1990). Although the frequencies of the SMMR were higher than desired for soil moisture monitoring, the need for soil moisture measurements from space focused attention on developing soil moisture retrieval techniques for follow-on sensors to the SMMR, such as the AMSR and CMIS, and dedicated soil moisture missions, such as HYDROS (Table 5). These mission applications trace their heritage to the initial observations of phenomenology and algorithm development using SMMR data.

SMMR data have been used successfully in numerous other multidisciplinary geophysical studies, attesting to the variety of scientific discoveries and advances made possible by the SMMR. A summary of the early results from the Seasat SMMR is provided by Lipes et al. (1979), and from the Nimbus-7 SMMR, it was provided by Gloersen et al. (1984). A compendium of later papers, and references to other research incorporating some key contributions of the SMMR to global change studies, was provided in the atlas of satellite observations edited by Gurney et al. (1993).

5. Synthetic aperture radar (SAR)

5.1. Instrument characteristics, heritage, and legacy instruments

The Seasat SAR was an L-band HH instrument that operated at a fixed range of incidence angles between 20° and 26° which resulted in a 100-km swath (Tables 7 and 8). The fine resolution data provided the first detailed images of the Earth not affected by clouds or darkness. The instantaneous data rate of 120 Mbps of the SAR exceeded the capabilities of available onboard tape recorders of that era and could only be collected when the satellite was in view of specially equipped ground stations. NASA supplied stations near Fairbanks, AK; Cape Canaveral, FL; and Goldstone, CA. The Canadian Centre for Remote Sensing

Table 7
SAR summary (Glackin, 2004; Glackin & Peltzer, 1999; Kramer, 2001)

Platform	Instrument	Country or agency	Band	Frequency (GHz)	Polarization	Best spatial res (m)	Swath width (km)	Orbit alt (km)	Launch date
Seasat	SAR	USA	L	1.28	HH	25	100	799	June 1978
SIR-A	SAR	USA	L	1.28	HH	40	50	260	November 1981
SIR-B	SAR	USA	L	1.28	HH	25	30	225	October 1984
Kosmos-1870	SAR	Russia	S	3.12	HH	25	20–35	275	July 1987
Almaz-1a	SAR	Russia	S	3.12	HH	13	2×172	~325	March 1991
ERS-1	AMI (SAR)	Europe	C	5.3	VV	30	100	784	July 1991
JERS-1	SAR	Japan	L	1.27	HH	18	75	570	February 1992
SIR-C/XSAR	SIR-C	USA	L, C	1.28, 5.3	VV, HH, HV, VH	30	10–200	225	1) April 1994
	X-SAR	Germany/ Italy	X	9.6	HH				2) September 1994
ERS-2	AMI (SAR)	Europe	C	5.3	VV	30	100	784	April 1995
RADARSAT-1	SAR	Canada	C	5.3	HH	10	100–170	798	November 1995
Mir-Priroda	Travers	Russia	L, S	1.28,3.28	VV, HH	50	50	400	April 1996
SRTM	C-SAR	USA	C	5.3	VV, HH	30	50–225	225	February 2000
	X-SAR	Germany/ Italy	X	9.6	HH				
ENVISAT	ASAR	Europe	C	5.33	VV, HH, VV/HH, HV/HH, VH/VV	30	100	800	March 2002
ALOS	PALSAR	Japan	L	1.27	VV, HH, HH/ HV,VV/VH	10	70	700	2005[a]
RADARSAT-2	SAR	Canada	C	5.3	Quad-pol	3	10–500	800	2005[a]
COSMO/ SkyMed Series	SAR-2000	Italy/France	X	9.6	VV, HH	1	10–200	616	2005–2007[a]
SAOCOM-1a	SAR	Argentina/ Italy	L			7	50–400		2005[a]
TerraSAR-X	X-SAR	Germany/ UK	X	9.6	various	1	~50	660	2006[a]
CEMD-SAR Series	SAR	China				4	25–125		2005+[a]
RISAT	SAR	India	C					609	2006[a]

[a] Estimated.

(CCRS) provided a station in St. Johns, Newfoundland, and the European Space Agency (ESA) provided a station near London in the United Kingdom. Coverage was thus obtained primarily over North America and portions of Western Europe. Based on the results of Seasat for both ocean and land surface mapping, SARs were selected to be flown on the space shuttle, including NASA's Shuttle Imaging Radar-A (SIR-A) in 1981, a single channel L-band HH SAR with optical data recording (Elachi et al., 1982), and SIR-B in 1984 (Cimino et al., 1986), also a single channel L-band HH SAR but with variable incidence angles and digital recording (Table 7).

Table 8
Seasat SAR summary (Jordan, 1980)

Satellite altitude	800 km
Frequency	1.28 GHz (L-band)
Polarization	HH
Spatial resolution	25×25 m
Swath width	100 km (spans 240–340 km on one side of S/C)
Antenna dimensions	10.74×2.16 m
Antenna type	Phased array, 8 microstrip panels
Antenna gain	35 dB
RF bandwidth	19 MHz
Transmit pulse length	33.4 μs
Pulse repetition freq	1463–1640 pps
Transmitter peak power	1000 W
Transmitter avg power	55 W
Data processing	Optical (digital for selected areas)

The next spaceborne SARs were from Russia and operated at S-band with HH polarization. European Space Agency's (ESA) ERS-1 was launched in 1991, with a C-band vertical transmit-vertical receive (VV) polarization SAR with a Seasat-like 100-km swath and 20–26° range of incidence angles. This highly successful mission was continued with ERS-2 in 1995. ESA's follow-on mission is ENVISAT, which was launched in March 2002. It carries a C-band dual-polarization system with swath widths varying between 100 and 400 km (Attema, 1991; Desnos et al., 2000). The Canadian Space Agency's RADARSAT-1,

a C-band HH system available at varying incidence angles, resolutions, and swath widths (40–500 km), was launched in 1995 and continues to provide valuable images into 2004.

The Japanese Space Agency flew the L-band HH JERS-1 SAR from 1992 to 1998, which had a more land-oriented set of fixed incidence angles of 32–38°. The next mission in this series is planned to be PALSAR to be launched onboard ALOS in 2005. It will be an L-band system with multiple polarizations, resolutions, look angles, and swath widths. In between ERS-1 and JERS-1, the joint NASA/German Space Agency/Italian Space Agency mission, Shuttle Imaging Radar-C/X-band SAR (SIR-C/X-SAR), flew twice in 1994. This three-frequency (L/C/X bands), fully polarimetric system (HH/VV/HV/VH for L/C, and VV for X) provided the most extensive spaceborne multiparameter radar data set available to date (Evans et al., 1997; Holt, 1998; Stofan et al., 1995).

In February 2000, Space Shuttle Endeavour carried the Shuttle Radar Topography Mission (SRTM) based on the SIR-C/X-SAR hardware, which has produced the most complete, highest resolution digital topographic map of Earth ever made. SRTM is a cooperative project between NASA and the National Imagery and Mapping Agency (NIMA) of the U.S. Department of Defense. The German and Italian Space Agencies provided an additional X-band interferometer as well. The mission was designed to use a single-pass C-band radar interferometer to produce a digital elevation model (DEM) of the Earth's land surface between about 60° north and 56° south latitude. The DEM has a 30-m pixel spacing and better than 10 m vertical accuracy (Farr & Kobrick, 2000).

Finally, an L-band InSAR mission is proposed as part of the EarthScope program (a partnership of the National Science Foundation, US Geological Survey and NASA). This mission is deemed as an essential capability to accomplish key objectives of Earth science and disaster management by the National Research Council (Committee on the Review of Earthscope Science Objectives and Implementation Planning, 2001). An InSAR mission is also the highest priority recommended by the Solid Earth Science Working Group chartered by NASA to define a 25-year vision for the Earth Science Enterprise (Solomon et al., 2004). An initial dedicated InSAR mission would provide coverage over Earth's most tectonically active regions. These data would be assimilated into models in a similar way to altimeter measurements over the ocean leading to an improvement in the understanding of the Earth's crust and response to the buildup of stress (Fig. 5).

5.2. SAR geophysical measurements

5.2.1. Oceans

Prior to Seasat, surface and internal waves were seen in airborne SAR data (e.g., Elachi, 1978; Elachi & Apel, 1976). Seasat SAR images revealed a number of ocean features if not for the first time, at least the most extensively, including current boundaries, eddies over a wide range of scales (10–400 km), temperature fronts, shoaling bathymetry, and atmospheric patterns related to storms, roll vortices, and rain cells (e.g., Beal et al., 1981; Fu & Holt, 1982; Vesecky & Stewart, 1982). Detection of surface waves was a primary science focus but this was soon found to be problematic due to nonlinearities arising from wave motion during the image formation process. Extensive research took place to understand and ultimately alleviate the nonlinearities, making considerable use of the SIR-B ocean imagery that was not subject to nonlinear imaging because of its lower platform altitude. Eventually, corrections were put

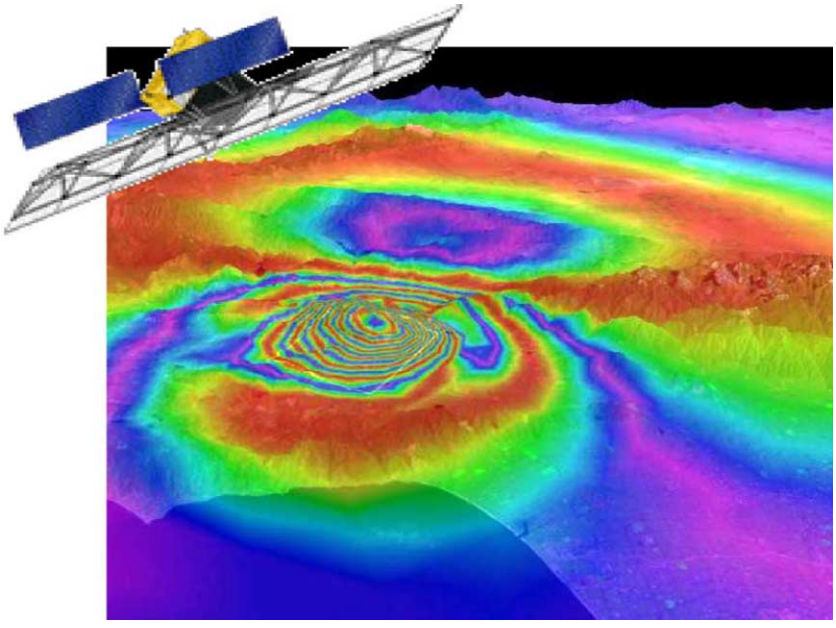

Fig. 5. Artist's conception of a dedicated L-band InSAR mission.

into place for the SAR wave mode products on ERS-1/2 and now for ENVISAT ASAR as well, which has the additional improvement of retrieving unambiguous wave direction. Another key science ocean product developed recently, SAR wind speed and direction, was first examined using Seasat SAR imagery and verified with coincident SASS products (Gerling, 1986). A C-band wind retrieval algorithm was developed with the ERS-1 scatterometer (Stoffelen & Anderson, 1997), which shared the same electronics package as the SAR, and thus could be directly applied to the SAR imagery as well. Making use of the wide swath of RADARSAT required deriving accurate conversion of the algorithm from the VV polarization of ERS-1/2 to RADARSAT's HH polarization. The fine resolution wind speeds from SAR imagery are particularly useful within coastal regions (Monaldo et al., 2001), providing a powerful complement to scatterometer winds which to date are not useful within at least a 25-km proximity to land.

In addition to waves and winds, ocean observations started with Seasat SAR have continued with all follow-on missions and have included most of the world's energetic and dynamic ocean regions (Holt, 2004). Detailed studies of currents, fronts, and eddies on all scales have been done within the major eastern and western boundary current regions as well as within the coastal zones which are highly variable in terms of circulation and winds and also subject to anthropogenic impacts of pollution. The value of SAR used in conjunction with other imaging ocean sensors, particularly those that measure sea-surface temperature, has been aptly demonstrated as well, to extend current and eddy detection during cloudy periods when optical and near-infrared sensors are not useful (e.g., DiGiacomo & Holt, 2001; Fu & Holt, 1983; Johannessen et al., 1996). There has been increasing interest in using SAR to examine marine boundary layer atmospheric features and storm events which produce characteristic imprints on ocean surface roughness (Beal & Pichel, 2000). The sensitivity of SAR to reduction of backscatter caused by surface oil slicks, both from natural biogenic sources and from hydrocarbons released by seeps, spills, or river/stormwater discharge, has also been extensively demonstrated (e.g., Masuko & Inomata, 1988; Wismann et al., 1993). SAR satellites are routinely tasked to monitor oil spill accidents and illegal ship discharge. A key issue in extending the value of SAR for oceanography is the need to improve temporal sampling to provide at least daily coverage (Holt & Hilland, 2000). Various options include the use of multiple SAR platforms, moving to higher (1400 km) than normal (600–800 km) orbital altitude to widen swath while maintaining a shallow range of incidence angles preferred for ocean backscatter, and even carrying two SAR antennas on a single platform. Daily coverage would provide repeat imaging at the scales of variability of the primary types of ocean features which SAR best observes as well as increase its value for operational ocean applications including coastal winds for input into forecasting models, ship traffic, oil spill tracking, and monitoring of fisheries.

5.2.2. Polar regions

Seasat SAR provided the first extensive fine resolution images of the western Arctic sea ice, enhanced by the 'collapse' of orbits in the polar regions which improves temporal sampling. The primary scientific value of the imagery was for deriving the most detailed sea ice motion maps ever produced, from which openings and closings of the ice cover clearly revealed where the largest heat exchange from the ocean to the air takes place (e.g., Carsey & Holt, 1987). These maps generated considerable interest, which led to the development of the first geophysical SAR product generation system, designed to automatically produce ice motion maps from ERS-1 SAR imagery (Holt et al., 1992; Kwok et al., 1990). Also included was identification of sea ice types, more readily identified with C-band data than on Seasat's L-band data, which is a proxy for sea ice thickness (Kwok et al., 1992). While the ice cover sampling was still piecemeal rather than broad, the value of these products was considerable and led to the next generation of ice motion product to be produced, making use of the wide swath capability of RADARSAT-1 from which complete coverage maps of the entire Arctic Ocean repeated every 3–6 days have been continuously obtained since October 1996. Included in this second-generation product system was the addition of a very significant tracking enhancement, going from Eulerian to Lagrangian tracking (Kwok et al., 1995). By tracking a grid element continuously over time, not only could the detailed deformation of that element be tracked, but the age of any newly formed ice could be tracked as well. This age tracking is used to derive first year ice thickness and thereby account for a major component of the mass balance of sea ice, which has been found to vary annually and in relation to the overall transport of ice within and out of the Arctic (Kwok & Cunningham, 2002). The deformation details of the motion maps have proven to be of considerable value for ice mechanics studies as well. The ice typing value of the imagery itself has significantly improved the ice charts developed for operations by the U.S. and foreign ice centers (Bertoia et al., 1998).

There was limited coverage of Greenland and northern glaciers from the Seasat SAR, but the value of SAR data for ice sheets and glaciers increased significantly when InSAR processing was applied to ERS-1 SAR data to derive ice sheet velocity fields (Goldstein et al., 1993). These velocity fields were more detailed than could be derived from any field measurements and also provided insight to subsurface location of grounding lines of ice shelves (Rignot & Jacobs, 2002). These measurements enabled assessments of snow accumulation rates, which have identified zones of Antarctica, that may have increasing or decreasing ice mass balance (Joughin et al., 2002; Rignot & Thomas, 2002). The most detailed maps of Antarctica ever made have resulted from two dedicated mapping missions with RADARSAT in 1997 and 2000 (Jezek, 1999; Jezek et al., 2003).

5.2.3. Land surface mapping

Seasat and subsequent SARs have demonstrated the potential to provide unique information about the health of the planet and its biodiversity, as well as critical data for natural hazards and resource assessments. Interferometric measurement capabilities demonstrated first with Seasat are now used to generate topographic maps, to monitor surface topographic change, and to monitor glacier ice velocity and ocean features (e.g., Madsen & Zebker, 1998; Zebker & Goldstein, 1986).

Seasat opened many eyes to the usefulness of imaging radar, even at steep incidence angles, for land surface studies (e.g., Ford, 1980; Ford et al., 1980). In the early 1970s, several researchers had begun work with radar images obtained from aircraft (Daily et al., 1978; Dellwig, 1969; Dellwig & Moore, 1966; MacDonald & Waite, 1973; Schaber et al., 1976). In particular, it was noted that radar images could be interpreted using techniques borrowed from aerial photography where the image tone and texture are the dominant sources of information. It was found that radar images were more sensitive to surface topographic variations, especially in heavily vegetated terrain, so that geologic structures could be mapped with some confidence. This coincided with the fact that radars could produce high-quality images through clouds as demonstrated first in Panama by Viskne et al. (1969), another characteristic of tropical areas (Ford, 1980).

Tone was another matter, as the strength of a radar return is mainly determined by the surface roughness. Several early studies sought to quantify the relationship between radar image tone and surface roughness, but the lack of calibrated radars made the results, while promising, more of a relative nature. When Seasat SAR data became available, several attempts were made to calibrate the images, ending with limited success (Held et al., 1983). Later, through extensive work with the AIRSAR testbed at JPL, calibrated radar images were finally produced and civilian orbital radars after Seasat have all been radiometrically calibrated. This has led to a much better understanding of the nature of radar scattering models and their use in predicting surface roughness from radar returns.

Building on the early measurements of surface roughness and the search for the connections between surface roughness and geological information, Farr (1992) measured the roughness of a number of lava flows in the Mojave Desert, finding that their surface roughness followed a predictable path of modification due to local geologic processes. Farr and Chadwick (1996) found a similar relationship for alluvial fans in China. As calibrated radar data and better scattering models became available, several investigators began an attempt to estimate near-surface soil moisture from its effect on the dielectric constant of the surface material (Ulaby et al., 1986). This is a much weaker effect on radar return, but progress has been made in certain environments. Recent work is centering on measuring deeper soil moisture with long-wavelength radars (e.g., Moghaddam et al., 2000).

A completely surprising variation on land surface mapping with radar came about when geologists familiar with the landscapes of southern Egypt were examining SIR-A images of the area. The images portrayed a landscape none of them had seen before—river valleys and their tributaries crossed tracts of land the geologists knew to be featureless sand sheets. Later, the answer became clear—the L-band radar had "seen" beneath several meters of extremely dry sand and imaged a buried landscape carved during previous wetter climatic periods up to 200,000 years ago (Elachi et al., 1984; McCauley et al., 1982, 1986; Schaber et al., 1986). Subsequently, SIR-B and SIR-C, as the next L-band orbital systems, were tasked to collect more images and the drainage networks were partially mapped. Currently, work is continuing using JERS-1, the only other L-band system to orbit, and will be followed with PALSAR data, when it is available (Paillou et al., 2003; Paillou & Rosenqvist, 2003).

The availability of multiple polarizations, particularly polarimetry, has brought many advances in the study of vegetation with imaging radar (e.g., Dobson et al., 1995; Evans et al., 1995; Morain & Simonett, 1967; Ranson et al., 1995). As the geometry of leaves, branches, and trunks is an important identifying characteristic of plants, polarization angles may be used to identify the plants and possibly their state of growth. The density of plants, known as the biomass, is an important environmental variable that radar sensors of various wavelengths can readily determine.

5.2.4. Planetary science

As imaging radar has proved itself for geologic applications on Earth, planetary scientists have used it at Venus and Titan and plans are being formulated for other planets. Cloud-shrouded Venus was mapped in the early 1980s by the Soviet Union and in the early 1990s by NASA with Magellan (Saunders & Pettengill, 1991). The entire planet, about the size of Earth, was mapped more than once by the Magellan SAR, and the altimeter and passive radiometer both collected global data sets as well. Titan, the largest moon of Saturn, will be visited by Cassini in 2004. As Titan is also cloud-covered, an imaging radar was included in the payload and will send back our first detailed views of its surface.

Proposals for future imaging radars include a radar with L-band or longer wavelength to map the surface of Mars (e.g., Campbell et al., 2004) and perhaps buried channels, and a long-wavelength radar or sounder to be sent to Europa to settle the question of whether it has a liquid ocean and how deep it is. Interferometric radar observations of these bodies may also be attempted, yielding additional information on their topography and possible surface changes.

6. Future directions

6.1. Improved spatial and temporal sampling

Chelton (2001) describes the importance of increased spatial sampling for altimetry observations. A Wide-Swath Ocean Altimeter (WSOA) has been developed for flight as an experiment on the follow-on to Jason-1, the Ocean Surface Topography Mission (OSTM). The WSOA will measure the range to the sea surface over a 200-km swath with the expected resolution of 15 km. The WSOA is based on the concept of radar interferometry. The instrument consists of two side-looking fan-beam antennas separated by a boom with a length of 5–10 m. Interferometry performed on the returned signals from the same targets on the ocean surface within a small off-nadir angle of incidence of about 4° yields SSH measurements across a swath width of about 200 km centered along the satellite ground track. This interferometric system would be used in conjunction with a dual frequency altimeter with a 3-frequency water vapor radiometer that would provide nadir observations and environmental corrections.

In addition to the Wide-Swath Ocean Altimeter, other methods described in Chelton (2001) for improving spatial sampling for altimetry include a low-cost altimeter constellation using 'Delay-Doppler' technology, a direct approach to obtaining high-resolution measurements of ocean topography by flying multiple altimeters in formation flight (Raney, 1998), and altimetry from Global Positioning System (GPS) reflections. The reflections of signals from the satellite constellation of the Global Positioning System (GPS) can be measured by a receiver on an earth-orbiting satellite to obtain altimetric measurements of ocean topography (e.g., Hajj & Zuffada, 2003; Martin-Neira et al., 2001). Over a 10-day period, a single receiver at an altitude of 400 km is capable of receiving about 12 reflections from any given 50 km cell on the earth's surface with the current constellation of 24 GPS satellites. Simulations indicate that a group of 8 optimally deployed low-power and low-cost receivers and multibeam high-gain antennas on satellites of opportunity could provide 10-day maps of SSH with an rms accuracy of 6 cm and a resolution of 25 km. Receivers mounted on the ground at some elevation (~200 m) have also been demonstrated to be useful for monitoring sea-level variations in the coastal regions.

Investigations into improvements in spatial samplings for scatterometers and SAR have included constellations as well as observations from Medium Earth Orbit (MEO) and Geosynchronous Orbit (GEO). A scatterometer in an MEO orbit would provide the improved revisit time required to increase the fidelity of operational weather forecasts for quickly evolving phenomena, such as storms, as well as to allow climate researchers to resolve diurnal and local inertial period variability that drive ocean mixing and transport processes. The improved revisit time could be accomplished by significantly increasing the effective swath width of the scatterometer system due to higher orbit altitude. Improved spatial resolution would allow meteorologists and oceanographers to observe fine scale wind features in coastal zones, tropical storms, fronts and squall lines. To accomplish this higher-resolution capability, larger antenna technology, as well as the addition of SAR techniques, are being examined as means to improve the spatial resolution of scatterometer measurements. Recently, a polarimetric radiometer, WindSat, was launched to measure ocean winds. This technique requires isolation of the various contributions to sea-surface emission for wind speed and direction.

A constellation of InSAR satellites is needed to address the requirements for monitoring a spectrum of steady and transient deformation processes associated with natural hazards, such as earthquakes. To ensure the ability to access any area on the surface of the Earth within 24 h would require two LEO satellites in orbits above 1000 km. MEO or GEO satellites would be equivalent to many spacecraft in LEO and would fully characterize the known transient processes, such as postseismic relaxation, slow earthquakes, creep events, and accelerated slip, with full global coverage. SAR missions in MEO or GEO would place a significant demand on the spacecraft resources (mass, power, data rate) and revolutionary antenna technologies would be required. High-efficiency integrated (single-chip) T/R modules would be necessary to ensure the mass, power, and costs of the modules are not prohibitively high when thousands of modules are required. Adaptive scanning and phase self-compensation techniques will be necessary to alleviate requirements on antenna flatness. Modular or distributed architectures will enable these systems to be very flexible. Radiation-tolerant electronics are also a major challenge, particularly for the antenna electronics, which have only limited shielding.

6.2. Combined active/passive measurements

The applications of scatterometer data to tropical storm tracking are described by Katsaros and Brown (1991). Tropical cyclones are devastating when they are accompanied by strong winds and heavy rain. The coincident measurement of wind vectors by the scatterometer and rain by microwave radiometer may reveal the interplay between the dynamics and the hydrologic balances of the storm. When applied to Hurricane Floyd, the high spatial resolution of ocean surface winds measured by QuikSCAT improves computation of the moisture transport, the vertical profiles of moisture sinking and diabatic heating, and the difference between evaporation and rain rate at the surface. Surface winds feed moisture into the hurricane. The moisture turns into rain, releases latent heat, and fuels the storm. Future missions focused on improved hurricane tracking can take advantage of this increase capability. In order to acquire more accurate winds under "extreme conditions"—i.e., high winds and rain, the addition of a multifrequency polarimetric radiometer capability with

coincident footprints could be used to augment the active radar scatterometer measurements. Radiometer channels would provide rain correction to the scatterometer-derived winds, as well as to improve wind accuracy performance across the entire swath.

Combined active and passive measurements are also being planned for soil moisture and ocean salinity sensing. These applications require low-frequency microwave measurements (L-band) for adequate parameter sensitivity and the measurement systems therefore require large antennas to achieve adequate spatial resolution. In addition, measurement of ocean salinity requires high radiometric precision and calibration stability. The radar complements the radiometer in these active/passive systems by providing improved spatial resolution (for soil moisture measurement) and a surface roughness correction (for ocean salinity measurement). New technologies, instrument concepts, and retrieval algorithms have been developed for these measurements (Njoku et al., 2000; Yueh et al., 2001) leading to the HYDROS (Entekhabi et al., 2003) and the Aquarius mission (Koblinsky et al., 2003). Concept studies are also in progress for a future mission that would combine active and passive sensors for measurement of snow properties.

6.3. Along-track interferometry

Along-track interferometry (ATI) is a unique SAR configuration that enables the velocity of the moving ocean surface to be measured over a very short time interval. Such data have been examined for deriving wave spectra and current velocity, to date primarily from aircraft platforms (Goldstein & Zebker, 1987; Goldstein et al., 1989). By careful tracking of multiple SAR observations of a single target on the ocean surface, the displacement or motion of the target can be determined by measuring the phase difference between the observations, after removal of other systematic motions. Such detailed measurements of ocean surface currents on a daily basis would be of considerable value both in highly dynamic coastal zones, where it is difficult to measure the complex current field either synoptically by spacecraft or with in situ sensors, and to provide a boundary condition for global sea-surface topography measurements from altimetry. However, more understanding particularly of the relationship between this surface measurement and deeper current fields is needed before implementation. Nominally for ATI, the platform is configured with a fore and aft radar antenna along the fuselage or platform velocity direction, where either one or both antennas transmit and both antennas receive the returns with a conventional side-looking radar beam. Aside from the general difficulty of sorting out the various contributions to the target motion as well as the systematic contributions from the platform and processing, one of the drawbacks of the nominal, side-looking two-antenna system is that only the line-of-sight radial component of the motion field is derived during a single imaging event. The full surface motion vector would thus require at minimum two perpendicular crossing acquisitions with minimal separation in time to avoid further ocean decorrelation. Recent studies have examined the concept of a pair of beams using dual antennas to squint forward and squint aft (dual aspect) of the nominal side-looking antenna beam (Frasier & Camps, 2001; Moller et al., 1998). By aligning these measurements, the full surface velocity vector may be obtained within a single acquisition. Such a concept might be particularly adaptable to a spaceborne system and even perhaps by using a split-beam single antenna, thus enabling current/motion measurements from a single spacecraft. An alternate concept, across-track interferometry has been recently demonstrated that can produce a digital elevation map of the ocean surface height, useful for measuring waves (Schulz-Stellenfleth et al., 2001) and mesoscale eddies (Fu, 2003). Another alternate concept to provide surface current estimates is to use line-of-sight SAR Doppler measurements over the ocean, which is being explored through use of the Wave Mode on the ENVISAT ASAR (Chapron et al., 2004).

6.4. Use of long radar wavelengths

SAR measurements at long wavelengths (approximately 1 m) have demonstrated an increased penetration of radar waves in vegetation and soil for mapping subcanopy and subsurface structures, and with an enhanced sensitivity to moisture and salinity (Hoekman & Quinones, 2000; Moghaddam et al., 2000; Paloscia, 2002; Rignot et al., 1995; Saatchi & Moghaddam, 2000). This capability makes SAR systems operating at these wavelengths the most promising tool for global inventory of forest biomass and the most relevant remote sensing measurement for NASA's Carbon Cycle Roadmap (Houghton, 2003). Until recently, such measurements were only possible from airborne sensors because suitable frequencies were not allocated for use for spaceborne applications. In July 2003, during the last World Radio Communication Conference in Geneva, a 6-MHz bandwidth allocation at P-band (435 MHz) was approved for spaceborne Earth observation, providing a unique opportunity for new missions (Recommendation ITU, 2003).

P-band measurements from space (1) will allow the quantitative assessment of global sources and sinks of terrestrial carbon and their geographical distributions, (2) will provide estimates of carbon stock (biomass) in forested ecosystems in boreal and temperate regions and improves the uncertainties in tropics, and (3) will provide high resolution and frequent observation of changes of carbon as a result of natural and anthropogenic disturbances, recovery processes, and management activities. The global measurement and monitoring capability of forest structure and biomass can contribute to the understanding of global carbon cycle and can be integrated into solutions that directly support local, national, and global decision-making.

7. Summary

Looking back after the 25th anniversary of the launch of Seasat, it is clear that its legacy as the first combined active–passive microwave mission is extensive. While it primarily was designed to focus on improving the knowledge of the dynamic global oceans, Seasat demonstrated the value of active radar data in combination with passive microwave data for a wide range of science disciplines that seek to improve the knowledge of Earth as a system. Despite Seasat's compelling legacy, much remains to be learned about the Earth that will improve our knowledge and understanding of the coupled atmosphere/ocean/land/ice system, that will allow us to better predict future environmental changes and there implications for life on Earth.

Acknowledgments

Work performed at the Jet Propulsion Laboratory, California Institute of Technology, is under contract with National Aeronautics and Space Administration. We wish to acknowledge the valuable contributions to the International Geoscience and Remote Sensing Symposium (IGARSS' 2003) Seasat special session of Tom Allan and Craig Dobson, and the additional comments to the manuscript by Lee Leung Fu and three anonymous reviewers. As with all spaceborne missions, Seasat was only accomplished through the contributions of many dedicated team members working toward the implementation of a unique vision.

References

Abdel-Messeh, M., & Quegan, S. (2000, Jul.). Variability in ERS scatterometer measurements over land. *IIEEE T Geosci Remote*, *38*(4), 1767–1776 (Part 2).

Alishouse, J. C. (1983). Total precipitable water and rainfall determinations from Seasat Scanning Multichannel Microwave Radiometer (SMMR). *Journal of Geophysical Research*, *88*, 1929–1935.

Atlas, R., Hoffman, R. N., Leidner, S. M., Sienkiewicz, J., Yu, T. W., Bloom, S. C., et al. (2001, Sept.). The effects of marine winds from scatterometer data on weather analysis and forecasting. *Bulletin of the American Meteorological Society*, *82*(9), 1965–1990.

Attema, E. P. W. (1991). The active microwave instrument on-board the ERS-1 satellite. *Proceedings of the I.E.E.E.*, *79*(6), 791–799.

Beal, R. C., DeLeonibus, P. S., & Katz, I. (1981). *Spaceborne synthetic aperture radar for oceanography* (p. 215). The Johns Hopkins University Press.

Beal, R. C., & Pichel, W. G. (2000). Coastal and marine applications of wide swath SAR. *Johns Hopkins APL Technical Digest*, *21*(1), 184.

Bernstein, R. L., & Morris, J. H. (1983). Tropical and midlatitude north pacific sea surface temperature variability from the Seasat SMMR. *Journal of Geophysical Research*, *88*, 1877–1891.

Bertoia, C., Falkingham, J., & Fetterer, F. (1998). Polar SAR data for operational sea ice mapping. In R. Kwok, & C. Tsatsoulis (Eds.), *Recent advances in the analysis of SAR data of the polar oceans* (pp. 201–234). Berlin: Springer Verlag.

Bingham, A. W., & Drinkwater, M. R. (2000, July). Recent changes in the microwave scattering properties of the Antarctic ice sheet. *IEEE Transactions on Geoscience and Remote Sensing*, *38*(4), 1810–1820.

Black, P. G., Gentry, R. C., Cardone, V. J., & Hawkins, J. D. (1985). Seasat microwave wind and rain observations in severe tropical and midlatitude marine storms. *Advances in Geophysics*, *27*, 198–227.

Brakenridge, G. R., Carlos, H. A., Nghiem, S. V., & Anderson, E. (2002). QuikSCAT/SeaWinds monitoring of large seasonal wetlands. American Geophysical Union Fall Meeting, San Francisco, CA, 6–10, December.

Campbell, B. A., Maxwell, T. A., & Freeman, A. (2004, Jul 23). Mars orbital synthetic aperture radar: Obtaining geologic information from radar polarimetry. *Journal of Geophysical Research, [Planets]*, *109*(E7).

Carsey, F. D. (1985). Summer Arctic sea ice characteristics from satellite microwave data. *Journal of Geophysical Research*, *90*(NC3), 5015–5034.

Carsey, F., & Holt, B. (1987, June 30). Beaufort-Chukchi ice margin data from Seasat-ice motion. *Journal of Geophysical Research*, *92*(C7), 7163–7172.

Carsey, F., & Pihos, G. (1989). Beaufort-Chukchi ice margin data from Seasat for ice conditions analogous to those of the Labrador Sea. *IEEE Transactions on Geoscience and Remote Sensing*, *27*, 41–551.

Chapron, B., Collard, F., & Kerbaol, V. (2004). Satellite synthetic aperture radar sea surface Doppler measurements. *Proceedings of the Second Workshop on Coastal and Marine Applications of SAR, 8–12 September 2003, Svalbard, Norway ESA Pub. SP-565* (pp. 133–140).

Chelton, D. B. (2001, Oct.). *Report of the High-Resolution Ocean Topography Science Working Group Meeting*. Corvallis, OR: College of Oceanic and Atmospheric Sciences Oregon State University. Ref. 2001-4.

Chelton, D. B., Hussey, K. J., & Parke, M. E. (1981). Global satellite measurements of water vapor, wind speed and wave height. *Nature*, *294*, 529–532.

Cheney, R. E., & Marsh, J. G. (1981). Seasat altimeter observations of dynamic topography in the gulf-stream region. *Journal of Geophysical Research*, *86*, 473–483.

Cheney, R. E., Marsh, J. G., & Beckley, B. D. (1983). Global mesoscale variability from collinear tracks of Seasat altimeter data. *Journal of Geophysical Research*, *88*, 4343–4354.

Choudhury, B. J., Wang, J. R., Hsu, A. Y., & Chien, Y. L. (1990). Simulated and observed 37 GHz emission over Africa. *International Journal of Remote Sensing*, *11*, 1837–1868.

Cimino, J., Elachi, C., & Settle, M. (1986). SIR-B—The 2nd shuttle imaging radar experiment. *IEEE Transactions on Geoscience and Remote Sensing*, *24*(4), 445–452.

Comiso, J. C. (2002, Oct. 15). A rapidly declining perennial sea ice cover in the Arctic. *Geophysical Research Letters*, *29*(20).

Committee on the Review of Earthscope Science Objectives and Implementation Planning, "Review of Earthscope Integrated Science, National Research Council, National Academy of Sciences, 2001.

Cunningham, J. D., Nelson, C. S., & Glackin, D. L. (2004). NPOESS: The U.S. environmental observing mission of the future and NOAA/EUMETSAT cooperation. Vancouver, Canada: International Astronautical Congress.

Daily, M., Elachi, C., Farr, T., & Schaber, G. (1978). Discrimination of geologic units in Death Valley using dual frequency and polarization imaging radar data. *Geophysical Research Letters*, *5*, 889–892.

Dellwig, L. F. (1969). An evaluation of multifrequency radar imagery of the Pisgah Crater Area, California. *Modern Geology*, *1*, 65–73.

Dellwig, L. F., & Moore, R. K. (1966). The geological value of simultaneously produced like-and cross-polarized radar imagery. *Journal of Geophysical Research*, *71*, 3597–3601.

De Mey, P., & Menard, Y. (1989). Synoptic analysis and dynamical adjustment of geos-3 and Seasat altimeter eddy fields in the Northwest Atlantic. *Journal of Geophysical Research*, *94*, 6221–6230.

Desnos, Y. -L., Buck, C., Guijarro, J., Suchail, J. -L., Torres, R., & Attema, E. (2000). The ENVISAT advanced synthetic aperture radar system. *Proceedings of IGARSS2000*, *1*, 1171–1173.

DiGiacomo, P. M., & Holt, B. (2001). Satellite observations of small coastal ocean eddies in the Southern California Bight. *Journal of Geophysical Research*, *106*(C10), 22521–22544.

Dobson, M. C., Ulaby, F. T., Pierce, L. E., Sharik, T. L., Bergen, K. M., Kellndorfer, J., et al. (1995, July). Estimation of forest biophysical characteristics in Northern Michigan with SIR-C/X-SAR. *IEEE Transactions on Geoscience and Remote Sensing*, *33*(4), 877–895.

Drinkwater, M. R., Long, D. G., & Bingham, A. W. (2001, Dec. 27). Greenland snow accumulation estimates from satellite radar scatterometer data. *Journal of Geophysical Research*, *106*(D24), 33935–33950.

Elachi, C. (1978). Radar imaging of the ocean surface. *Boundary-Layer Meteorology*, *13*, 165–179.

Elachi, C., & Apel, J. (1976). Internal wave observations made with an airborne synthetic aperture imaging radar. *Geophysical Research Letters*, *3*, 647–650.

Elachi, C., Brown, W. E., Cimino, J. B., Dixon, T., Evans, D. L., Ford, J. P., et al. (1982). Shuttle imaging radar experiment. *Science*, *218*, 996–1004.

Elachi, C., Roth, L. E., & Schaber, G. G. (1984). Spaceborne radar subsurface imaging in hyperarid regions. *IEEE Transactions on Geoscience and Remote Sensing*, *GE-22*, 383–388.

Entekhabi, D., Smith, J., Spencer, M., & Girard, R. (2003, July). The hydrosphere state mission: An overview. *Geoscience and Remote Sensing Symposium, 2003, IGARSS '03. Proceedings. 2003. IEEE International*, *vol. 3, 21–25*. (pp. 1894–1897).

Evans, D., Kasischke, E., Melack, J., Dozier, J., van Zyl, J., Apel, J., et al. (1995). Spaceborne synthetic aperture radar: Current status and future directions. *NASA Technical Memorandum*, *4679*, 171.

Evans, D. L., Plaut, J. J., & Stofan, E. R. (1997, Feb). Overview of the spaceborne imaging Radar-C/X-band synthetic aperture radar (SIR-C/S-SAR) missions. *Remote Sensing of Environment*, *59*(2), 135–140.

Farr, T. G. (1992). Microtopographic evolution of lava flows at Cima Volcanic Field, Mojave Desert, California. *Journal of Geophysical Research*, *97*, 15171–15179.

Farr, T. G., & Chadwick, O. A. (1996). Geomorphic processes and remote sensing signatures of alluvial fans in the Kun Lun Mountains, China. *Journal of Geophysical Research*, *101*, 23091–23100.

Farr, T. G., & Kobrick, M. (2000, Nov. 28). Shuttle radar topography mission produces a wealth of data. *Eos, Transactions-American Geophysical Union*, *81*(48), 583–585.

Ford, J. P. (1980). Seasat orbital radar imagery for geologic mapping: Tennessee–Kentucky–Virginia. *American Association of Petroleum Geologists Bulletin*, *64*, 2064–2094.

Ford, J. P., Blom, R. G., Bryan, M. L., Dailey, M. I., Dixon, T. H., Elachi, C., et al. (1980). *Seasat Views North America, The Caribbean, and Western Europe with Imaging Radar*, *vol. 80-67*. (pp. 361–370) Pasadena, CA: JPL Publication.

Foster, J. L., & Chang, A. T. C. (1993). Snow cover. In R. J. Gurney, J. L. Foster, & C. L. Parkinson (Eds.), *Atlas of satellite observations related to global change* (pp. 361–370). Cambridge University Press.

Frasier, S. J., & Camps, A. J. (2001). Dual-beam interferometry for ocean surface current vector mapping. *IEEE Transactions on Geoscience and Remote Sensing*, *39*(2), 401–414.

Fu, L. L. (1983). On the wave number spectrum of oceanic mesoscale variability observed by the Seasat altimeter. *Journal of Geophysical Research*, *88*(C7), 4331–4341.

Fu, L. -L. (Ed.). (2003). Wide-Swath Altimetric Measurement of Ocean Surface Topography. *JPL Publication 03–002* (pp. 67) Pasadena, CA: Jet Propulsion Laboratory.

Fu, L. -L, & Cazenave, A. (2001). Satellite altimetry and earth sciences: A handbook of techniques and applications. *International Geophysics Series*, *vol. 69*. (p. 200) San Diego, CA: Academic Press.

Fu, L. -L., & Holt, B. (1982). *Seasat Views Oceans and Sea Ice with Synthetic-Aperture Radar*, *vol. 81–120* (p. 200). Pasadena, CA: JPL Publication.

Fu, L. -L., & Holt, B. (1983). Some examples of detection of oceanic mesoscale eddies by the Seasat synthetic-aperture radar. *Journal of Geophysical Research*, *88*, 1844–1852.

Fu, L.-L., Stammer, D., Leben, R. R. & Chelton, D. B. (2003, July). "Improved Spatial Resolution of Ocean Surface Topography from the T/P–Jason-1 Altimeter Mission," in EOS, vol. 84, no. 26, pp. 241, 247–248.

Gerling, T. W. (1986). Structure of the surface wind field from the Seasat SAR. *Journal of Geophysical Research*, *91*, 2308–2320.

Glackin, D. L. (2004). Remote Sensing Satellite Database. The Aerospace Corporation, unpublished work based solely on open sources.

Glackin, D. L., & Peltzer, G. R. (1999). Civil, Commercial and International Remote Sensing Systems and Geoprocessing. El Segundo, CA: The Aerospace Press, and Reston, VA: AIAA.

Gloersen, P., & Barath, F. T. (1977). A scanning multichannel microwave radiometer for Nimbus-G and Seasat-A. *IEEE Journal of Oceanic Engineering*, *OE-2*, 172–178.

Gloersen, P., et al. (1984). A summary of results from the first nimbus-7 SMMR observations. *Journal of Geophysical Research*, *89*, 5335–5344.

Goldstein, R. M., Barnett, T. P., & Zebker, H. A. (1989). Remote sensing of ocean currents. *Science*, *246*, 1282–1285.

Goldstein, R. M., Engelhardt, H., Kamb, B., & Frolich, R. M. (1993). Satellite radar interferometry for monitoring ice sheet motion: Application to an Antarctic ice stream. *Science*, *262*, 1525–1530.

Goldstein, R. M., & Zebker, H. A. (1987). Interferometric radar measurement of ocean surface currents. *Nature*, *328*(6132), 707–709.

Gurney, R. J., Foster, J. L., & Parkinson, C. L. (Eds.). (1993). *Atlas of satellite observations related to global change* (p. 470). Cambridge: Cambridge University Press.

Hajj, G. A., & Zuffada, C. (2003, Oct 15). Theoretical description of a bistatic system for ocean altimetry using the GPS signal. *Radio Science*, *38*(5), 10.1–10.9 (art. no. 1089).

Hardin, P. J., & Jackson, M. W. (2003, Nov.). Investigating SeaWinds terrestrial backscatter: Equatorial savannas of South America. *Photogrammetric Engineering and Remote Sensing*, *69*(11), 1243–1254.

Held, D., Werner, C., & Wall, S. (1983). The absolute amplitude calibration of the Seasat synthetic aperture radar: An intercomparison with other l-band radar systems. *Abstract, IEEE Geosci. Rem. Sensing Symposium, San Francisco, CA*.

Hoekman, D. H., & Quinones, M. J. (2000). Land cover type and biomass classification using AirSAR data for evaluation of monitoring scenarios in the Colombian Amazon. *IEEE Transactions on Geoscience and Remote Sensing*, *38*(2), 685–696.

Hofer, R., Njoku, E. G., & Waters, J. W. (1981). Microwave radiometric measurements of sea surface temperature from the Seasat satellite: First results. *Science*, *212*, 1385–1387.

Holt, B. (1998). Introduction to special section: studies of the ocean surface from the spaceborne imaging radar-C/X-Band SAR experiments. *Journal of Geophysical Research*, *103*(C9), 18813–18814.

Holt, B. (2004). SAR imaging of the ocean surface. In C. R. Jackson, & J. R. Apel (Eds.), *Synthetic aperture radar marine user's manual* (pp. 25–81). Washington, DC: NOAA NESDIS Office of Research and Applications.

Holt, B., & Hilland, J. (2000). Rapid-repeat SAR imaging of the ocean surface: Are daily observations possible? *Johns Hopkins APL Technical Digest*, *vol. 21, no. 1*. (pp. 162–169).

Holt, B., Rothrock, D., & Kwok, R. (1992). Determination of sea ice motion from satellite images. In F. Carsey (Ed.), *Microwave remote sensing of sea ice*. *Geophysical Monograph*, *vol. 68* (pp. 343–354). Washington, DC: American Geophysical Union.

Houghton, R. A. (2003). Why are estimates of the terrestrial carbon balance so different? *Global Change Biology*, *9*(4), 500–509.

Jezek, K. C. (1999). Glaciological properties of the Antarctic ice sheet from RADARSAT-1 synthetic aperture radar imagery. *Annals of Glaciology*, *29*, 286–290.

Jezek, K. C., Farness, K., Carande, R., Wu X., X., & Labelle-Hamer, N. (2003, June 5). RADARSAT 1 synthetic aperture radar observations of

Antarctica: Modified Antarctic Mapping Mission, 2000. *Radio Science*, *38*(4) (art. no. 8067).

Johannessen, J. A., Shuchman, R. A., Digranes, G., Lyzenga, D. R., Wackerman, C., Johannessen, O. M., et al. (1996, Mar 15). Coastal ocean fronts and eddies imaged with ERS 1 synthetic aperture radar. *Journal of Geophysical Research*, *101*(C3), 6651–6667.

Johnson, J. W., Williams, L. A., Bracalente, E. M., Beck, F. B., & Grantham, W. L. (1980). Seasat-a satellite scatterometer instrument evaluation. *IEEE Journal of Oceanic Engineering*, *OE-5*(2), 138–144.

Jones, W. L., Schroeder, L. C., Boggs, D. H., Bracalante, E. M., Brown, R. A., Dome, G. J., et al. (1982). The SEASAT-A satellite scatterometer: The geophysical evaluation of remotely sensed wind vectors over the ocean. *Journal of Geophysical Research*, *87*, 3297–3317.

Jones, W. L., Wentz, F. J., & Schroeder, L. C. (1978, Nov–Dec). Algorithm for inferring wind stress from SeaSat-A. *AIAA Journal of Spacecraft and Rockets*, *15*(6), 368–374.

Jordan, R. L. (1980). The Seasat-A synthetic aperture radar system. *IEEE Journal of Oceanic Engineering*, *OE-5*(2), 154–163.

Joughin, I., Tulaczyk, S., Bindschadler, R., & Price, S. F. (2002, Nov.). Changes in West Antarctic ice stream velocities: Observation and analysis. *Journal of Geophysical Research*, *107*(B11).

Katsaros, K. B., & Brown, R. A. (1991). Legacy of the Seasat mission for studies of the atmosphere and air–sea–ice interactions. *Bulletin of the American Meteorological Society*, *72*, 967–981.

Kennett, R. G., & Li, F. K. (1989). Seasat over-land scatterometer data: Part I. Global overview of the Ku-band backscatter coefficients. *IEEE Transactions on Geoscience and Remote Sensing*, *27*(5), 592–605.

Kerr, Y. H., & Njoku, E. G. (1990). A semiempirical model for interpreting microwave emission from semiarid land surfaces as seen from space. *IEEE Transactions on Geoscience and Remote Sensing*, *28*, 384–393.

Kimball, J. S., McDonald, K. C., Keyser, A. R., Frolking, S., & Running, S. W. (2001, Jan.). Application of the NASA scatterometer (NSCAT) for determining the daily frozen and nonfrozen landscape of Alaska. *Remote Sensing of Environment*, *75*(1), 113–126.

Koblinsky, C. J., Hidebrand, P., LeVine, D., Pellerano, F., Chao, Y., Wilson, W., Yueh, S., et al. (2003). Sea surface salinity from space: Science goals and measurement approach. *Radio Science*, *38*(4), 8064.

Kramer, H. J. (2001). *Observation of the earth and its environment: Survey of missions and sensors* (4th ed.). Berlin: Springer-Verlag.

Kwok, R., & Cunningham, G. F. (2002, Sep–Oct). Seasonal ice area and volume production of the Arctic Ocean: November 1996 through April 1997. *Journal of Geophysical Research*, *107*(C10).

Kwok, R., Cunningham, G. F., & Yueh, S. (1999, Nov. 15). Area balance of the Arctic Ocean perennial ice zone: October 1996 to April 1997. *Journal of Geophysical Research, [Oceans]*, *104*(C11), 25747–25759.

Kwok, R., Curlander, J. C., McConnell, R., & Pang, S. S. (1990, Jan.). An ice-motion tracking system at the Alaska SAR facility. *IEEE Journal of Oceanic Engineering*, *15*(1), 44–54.

Kwok, R., Rignot, E., Holt, B., & Onstott, R. (1992, Feb. 15). Identification of sea ice types in spaceborne synthetic aperture radar data. *Journal of Geophysical Research*, *97*(C2), 2391–2402.

Kwok, R., Rothrock, D. A., Stern, H. L., & Cunningham, G. F. (1995, Mar.). Determination of the age distribution of sea–ice from Lagrangian observations of ice motion. *IEEE Transactions on Geoscience and Remote Sensing*, *33*(2), 392–400.

Laxon, S., Peacock, N., & Smith, D. (2003). High interannual variability of sea ice thickness in the Arctic region. *Nature*, *425*(6961), 947–950.

Lipes, R. G., Bernstein, R. L., Cardone, V. J., Katsaros, K. B., Njoku, E. G., Riley, A. L., et al. (1979). Seasat scanning multichannel microwave radiometer: results of the Gulf of Alaska workshop. *Science*, *204*, 1415–1417.

Liu, W. T. (2002). Progress in scatterometer application. *Journal of Oceanography*, *58*, 121–136.

Liu, W. T. (2003, 03–12 June). Scientific opportunities provided by seawinds in tandem. JPL Publication.

Liu, W. T., & Niiler, P. P. (1984). Determination of monthly mean humidity in the atmospheric surface layer over oceans from satellite data. *Journal of Physical Oceanography*, *14*, 1451–1457.

Long, D. G., Drinkwater, M. R., Holt, B., Saatchi, S., & Bertoia, C. (2001). Global ice and land climate studies using scatterometer image data. *EOS*, *82*, 503.

Long, D. G., & Hardin, P. J. (1994). Vegetation studies of the Amazon basin using enhanced resolution Seasat scatterometer data. *IEEE Transactions on Geoscience and Remote Sensing*, *32*, 449–460.

MacDonald, H. C., & Waite, W. P. (1973). Imaging radars provide terrain texture and roughness parameters in semi-arid environments. *Modern Geology*, *4*, 145–158.

Macelloni, G., Paloscia, S., Pampaloni, P., & Santi, E. (2003, June 20). Global scale monitoring of soil and vegetation using SSM/I and ERS wind scatterometer. *International Journal of Remote Sensing*, *24*(12), 2409–2425.

Madsen, S. N., & Zebker, H. A. (1998). Imaging radar interferometry. In F. M. Henderson, & A. J. Lewis (Eds.), *Principles and applications of imaging radar. Manual of Remote Sensing*, *vol. 2*. (pp. 866) New York: Wiley.

Magagi, R. D., & Kerr, Y. H. (2001). Estimating surface soil moisture and soil roughness from ERS-1 winscatterometer data over semi-arid area: Use of the co-poarisation ratio. *Remote Sensing of Environment*, 432–445.

Martin-Neira, M., Capparriri, M., Funt-Rosselo, J., Lannelongue, S., & Vallmitjana, C. S. (2001). The PARIS concept: An experimental demonstration of sea surface altimetery using GPS reflected signals. *IEEE Transactions on Geoscience and Remote Sensing*, *39*, 142–150.

Masuko, H., & Inomata, H. (1988). Observations of artificial slick by X and Ka band airborne scatterometers. *Digest IGARSS88*, *2*, 1089–1090.

Mazzega, P. (1985). M2 model of the global ocean tide derived from Seasat altimetry. *Marine Geodesy*, *9*, 335–363.

McCauley, J. F., Breed, C. S., Schaber, G. G., McHugh, W. P., Issawi, B., Haynes, C. V., et al. (1986). Paleodrainages of the Eastern Sahara—the Radar Rivers Revisited (SIR-A/B implications for a mid-Tertiary trans-African drainage system). *IEEE Transactions on Geoscience and Remote Sensing*, *GE-24*, 624–648.

McCauley, J. F., Schaber, G. G., Breed, C. S., Grolier, M. J., Haynes, C. V., Issawi, B., et al. (1982). Subsurface valleys and geoarchaeology of the Eastern Sahara revealed by shuttle radar. *Science*, *218*, 1004–1020.

McMurdie, L. A., & Katsaros, K. B. (1985). Atmospheric water distribution in a midlatitude cyclone observed by the Seasat scanning multichannel microwave radiometer. *Monthly Weather Review*, *113*, 584–598.

Menard, Y. (1983). Observations of Eddy fields in the Northwest Atlantic and Northwest Pacific by Seasat altimeter data. *Journal of Geophysical Research*, *88*(C3), 1853–1866.

Moghaddam, M., Saatchi, S., & Cuenca, R. H. (2000). Estimating subcanopy soil moisture with radar. *Journal of Geophysical Research*, *105*(D11), 14899–14911.

Mognard, N. M., Campbell, W. J., Cheney, R. E., & Marsh, J. (1983). Southern ocean mean monthly waves and surface winds for winter 1978 by Seasat radar altimeter. *Journal of Geophysical Research*, *88*(C3), 1736–1744.

Moller, D., Frasier, S. J., Porter, D. L., & McIntosh, R. E. (1998). Radar-derived interferometric surface currents and their relationship to subsurface current structure. *Journal of Geophysical Research*, *103*(C6), 12839–12852.

Monaldo, F. M., Thompson, D. R., Beal, R. C., Pichel, W. G., & Clemente-Colòn, P. (2001). Comparison of SAR-derived wind speed with model predictions and ocean buoy measurements. *IEEE Transactions on Geoscience and Remote Sensing*, *39*(12), 2587–2600.

Moore, R. K., & Fung, A. K. (1979). Radar determination of winds at sea. *Proceeding of the I.E.E.E.*, *67*, 1504–1521.

Moore, R. K., et al. (1974). Simultaneous active and passive microwave response of the earth—the Skylab Radscat Experiment. *Proc. 9th Intl. Symp. On Rem. Sens. of Environ., Ann Arbor, MI* (pp. 189–217).

Morain, S. A., & Simonett, D. S. (1967). K-Band radar in vegetation mapping. *Photogrammetric Engineering and Remote Sensing*, *33*, 730–740.

Naderi, F. M., Freilich, M. H., & Long, D. G. (1991). Spaceborne radar measurements of wind velocity over the ocean—An overview of the NSCAT scatterometer system. *Proceedings of the I.E.E.E.*, *79*(6), 850–866.

Nghiem, S. V., Barber, D. G., Brakenridge, G. R., Leshkevich, G. A., Markus, T., Neumann, G., et al. (2003, 8–12 December). Surface water applications of satellite scatterometry. *American Geophysical Union Fall Meeting*, San Francisco, CA.

Njoku, E. G. (1982). Passive microwave remote sensing of the earth from space—A review. *Proceedings of the I.E.E.E.*, *70*, 728–750.

Njoku, E. G., Stacey, J. M., & Barath, F. T. (1980). The Seasat scanning multichannel microwave radiometer (SMMR): Instrument description and performance. *IEEE Journal of Oceanic Engineering*, *OE-5*, 100–115.

Njoku, E. G., & Swanson, L. (1983). Global measurements of sea surface temperature, wind speed and atmospheric water content from satellite microwave radiometry. *Monthly Weather Review*, *111*, 1977–1987.

Njoku, E. G., Wilson, W. J., Yueh, S. H., & Rahmat-Samii, Y. (2000, Nov.). A large-antenna microwave radiometer–scatterometer concept for ocean salinity and soil moisture sensing. *IEEE Transactions on Geoscience and Remote Sensing*, *38*(6), 2645–2655.

Paillou, Ph., Grandjean, G., Baghdadi, N., Heggy, E., August-Bernex, T., & Achache, J. (2003). Subsurface imaging in south-central Egypt using low-frequency radar: Bir safsaf revisited. *IEEE Transactions on Geoscience and Remote Sensing*, *41*, 1672–1684.

Paillou, Ph., & Rosenqvist, A. (2003). SaharaSAR: A JERS-1 radar mosaic for subsurface geology mapping in east Sahara. *Abs., IEEE Geosci. Rem. Sens. Symp., Toulouse*.

Paloscia, S. (2002, Apr.). A summary of experimental results to assess the contribution of SAR for mapping vegetation biomass and soil moisture. *Canadian Journal of Remote Sensing*, *28*(2), 246–261.

Parkinson, C. L., & Cavalieri, D. J. (2002). A 21 year record of Arctic sea–ice extents and their regional, seasonal and monthly variability and trends. *Annals of Glaciology*, *34*, 441–446.

Parkinson, C. L., & Gloersen, P. (1993). Global sea ice coverage. In R. J. Gurney, J. L. Foster, & C. L. Parkinson (Eds.), *Atlas of satellite observations related to global change* (pp. 371–383). Cambridge University Press.

Raney, R. K. (1998). The Delay-Doppler radar altimeter. *IEEE Transactions on Geoscience and Remote Sensing*, *36*, 1578–1588.

Ranson, K. J., Saatchi, S., & Guoqing, Sun (1995, July). Boreal forest ecosystem characterization with SIR-C/XSAR. *IEEE Transactions on Geoscience and Remote Sensing*, *33*(4), 867–876.

Recommendation ITU R SA. 1260-1, "Feasibility of Sharing Between Active Spaceborne Sensors and Other Services in the Range 420–470 MHz," World Radio Communication Conference (WRC-03), Geneva, Switzerland, 9 June to 4 July, 2003.

Rignot, E., & Jacobs, S. S. (2002, Jun. 14). Rapid bottom melting widespread near Antarctic ice sheet grounding lines. *Science*, *296*(5575), 2020–2023.

Rignot, E., & Thomas, R. H. (2002, Aug. 30). Mass balance of polar ice sheets. *Science*, *297*(5586), 1502–1506.

Rignot, E. J., Zimmerman, R., & Van Zyl, J. J. (1995, Sept.). Spaceborne applications of P-band imaging radar for measuring forest biomass. *IEEE Transactions on Geoscience and Remote Sensing*, *33*(5), 1162–1169.

Saatchi, S., & Moghaddam, M. (2000, March). Estimation of crown and stem water content and biomass of boreal forest using polarimetric SAR imagery. *IEEE Transactions on Geoscience and Remote Sensing*, *38*(2), 697–709.

Saunders, R. S., & Pettengill, G. H. (1991). *Magellan: Mission Summary, Science, Special Issue on Magellan at Venus*, *252*, 247–248.

Schaber, G. G., Berlin, G. L., & Brown, W. E., Jr. (1976). Variations in surface roughness within Death Valley, California: Geologic evaluation of 25-cm-wavelength radar images. *Geological Society of America Bulletin*, *87*, 29–41.

Schaber, G. G., McCauley, J. F., Breed, C. S., & Olhoeft, G. R. (1986). Shuttle imaging radar: physical controls on signal penetration and subsurface scattering in the Eastern Sahara. *IEEE Transactions on Geoscience and Remote Sensing*, *GE-24*, 603–623.

Schroeder, L. C., Boggs, D. H., Dome, G., Halberstam, I. M., Jones, W. L., Pierson, W. J., et al. (1982). The relationship between wind vector and normalized radar cross section used to derive Seasat-A satellite scatterometer winds. *Journal of Geophysical Research*, *87*, 3318–3336.

Schulz-Stellenfleth, J., Horstmann, J., Lehner, S., & Rosenthal, W. (2001). Sea surface imaging with an across-track synthetic aperture radar: The SINEWAVE experiment. *IEEE Transactions on Geoscience and Remote Sensing*, *39*(9), 2017–2028.

Solomon, S. C., Bloxham, J., Donnellan, A., Elachi, C., Evans, D., Rignot, E., et al. (2004). A plan for living on a restless planet. *EOS, Transactions-American Geophysical Union*, *184*(45), 485–491.

Stewart, R. H. (1988). Seasat: Results of the mission. *Bulletin of the American Meteorological Society*, *69*, 1441–1447.

Stofan, E. R., Evans, D. L., Schmullius, C., Holt, B., Plaut, J. J., van Zyl, J., et al. (1995). Overview of results of spaceborne imaging radar-C, X-band synthetic aperture radar (SIR-C/X-SAR). *IEEE Transactions on Geoscience and Remote Sensing*, *33*, 817–828.

Stoffelen, A., & Anderson, D. (1997). Scatterometer data interpretation: Estimation and validation of the transfer function CMOD4. *Journal of Geophysical Research*, *102*(C3), 5767–5780.

Townsend, W. F. (1980). An initial assessment of the performance achieved by the Seasat-1 radar altimeter. *IEEE Journal of Oceanic Engineering*, *OE-5*(2), 80–92.

Ulaby, F., Fawwaz, T., Moore, Richard K., & Fung, Adrian K. (1986, January). Microwave remote sensing. *Fundamentals and Radiometry*, *vol. 1*. Artech House Books Remote Sensing Library.

Vesecky, J. F., & Stewart, R. H. (1982). Observations of the sea surface phenomena using imagery from the Seasat synthetic aperture radar: An assessment. *Journal of Geophysical Research*, *87*, 3397–3430.

Viskne, A., Liston, T. C., & Sapp, C. D. (1969). SLR reconnaisance of Panama. *Geophysics*, *34*, 54–64.

Wagner, W., Scipal, K., Pathe, C., Gerten, D., Lucht, W., & Rudolf, B. (2003). Evaluation of the agreement between the first global remotely sensed soil moisture data with model and precipitation data. *Journal of Geophysical Research, [Atmospheres]*, *108*(D19) (art. No. 4611).

Wentz, F. J. (1991). A simplified wind vector algorithm for satellite scatterometers. *Journal of Atmospheric and Oceanic Technology*, *8*(5), 697–704.

Wentz, F. J., Peteherych, S., & Thomas, L. A. (1984). A model function for ocean radar cross-sections at 14.6 GHz. *Journal of Geophysical Research*, *86*, 3689–3704.

Wilheit, T., Chang, A. T. C., & Milman, A. S. (1980). Atmospheric corrections to passive microwave observations of the ocean. *Boundary-Layer Meteorology*, *18*, 65–77.

Wingham, D. (1999). The first of the European space agency's opportunity missions: CryoSat. *Earth Observation Quarterly*, *63*, 21–24.

Wingham, D. J., Ridout, A. J., Scharroo, R., Arthern, R. J., & Shum, C. K. (1998). Antarctic elevation change 1992 to 1996. *Science*, *282*, 456–458.

Wismann, V. (2000a, Jul. 2). Monitoring of seasonal snowmelt on greenland with ERS scatterometer data. *IEEE Transactions on Geoscience and Remote Sensing*, *38*(4), 1821–1826.

Wismann, V. (2000b). Monitoring of seasonal thawing in Siberia with ERS scatterometer data. *IEEE Transactions on Geoscience and Remote Sensing*, *38*(4), 1804–1809.

Wismann, V., Gada, M., Alpers, W., & Hühnerfuss, H. (1993). The damping of short gravity-capillary waves by experimental sea slicks measured by an airborne multi-frequency microwave scatterometer. *Proc. Oceans '93, Victoria BC*, *vol. II*. (p. 342–347).

Woodhouse, I. H., & Hoekman, D. H. (2000). Determining land-surface parameters from the ERS wind scatterometer. *IEEE Transactions on Geoscience and Remote Sensing*, *38*(1), 126–140.

Wu, X. P., Watkins, M. M., Ivins, E. R., Kwok, R., Wang, P., & Wahr, J. M. (2002, Nov.). Toward global inverse solutions for current and past ice mass variations: Contribution of secular satellite gravity and topography change measurements. *Journal of Geophysical Research*, *107*(B11).

Wunsch, C., & Gaposchkin, M. (1980). On using satellite altimetry to determine the general circulation of the oceans with applications to geoid improvement. *Reviews of Geophysics and Space Physics*, *18*, 725–745.

Yueh, S. H., West, R., Wilson, W. J., Li, F. K., Njoku, E. G., & Rahmat-Samii, Y. (2001, May). Error sources and feasibility for microwave remote sensing of ocean surface salinity. *IEEE Transactions on Geosciences and Remote Sensing*, *39*(5), 1049–1060.

Zebker, H. A., & Goldstein, R. M. (1986). Topographic mapping from interferometric synthetic aperture radar observations. *Journal of Geophysical Research*, *91*, 4993–4999.

Zhao, Y. H., Liu, A. K., & Long, D. G. (2002, Jun.). Validation of sea ice motion from QuikSCAT with those from SSM/I and buoy. *IEEE Transactions on Geoscience and Remote Sensing*, *40*(6), 1241–1246.

Zwally, H. J., Beckley, M. A., Brenner, A. C., & Giovinetto, M. B. (2002a). Motion of major ice-shelf fronts in antarctica from slant-range analysis of radar altimeter data, 1978–98. *Annals of Glaciology*, *34*, 255–262.

Zwally, H. J., & Brenner, A. C. (2001). Ice sheet dynamics and mass balance. In L. -L. Fu, & A. Cazenave (Eds.), *Satellite altimetry and earth sciences: A handbook of techniques and applications*. *International Geophysics Series*, *vol. 69*. (pp. 351–369) San Diego, CA: Academic Press.

Zwally, H. J., Comiso, J. C., Parkinson, C. L., Cavalieri, D. J., & Gloersen, P. (2002b). Variability of Antarctic sea ice 1979–1998. *Journal of Geophysical Research*, *107*(C5) (art. no. 3041).